

REVIEW ARTICLE

Open Access

Heteronanostructural metal oxide-based gas microsensors

Lin Liu¹, Yingyi Wang^{1,2}, Yinhang Liu^{1,3}, Shuqi Wang¹, Tie Li¹, Simin Feng¹✉, Sujie Qin²✉ and Ting Zhang^{1,4,5,6,7}✉

Abstract

The development of high-performance, portable and miniaturized gas sensors has aroused increasing interest in the fields of environmental monitoring, security, medical diagnosis, and agriculture. Among different detection tools, metal oxide semiconductor (MOS)-based chemiresistive gas sensors are the most popular choice in commercial applications and have the advantages of high stability, low cost, and high sensitivity. One of the most important ways to further enhance the sensor performance is to construct MOS-based nanoscale heterojunctions (heteronanostructural MOSs) from MOS nanomaterials. However, the sensing mechanism of heteronanostructural MOS-based sensors is different from that of single MOS-based gas sensors in that it is fairly complex. The performance of the sensors is influenced by various parameters, including the physical and chemical properties of the sensing materials (e.g., grain size, density of defects, and oxygen vacancies of materials), working temperatures, and device structures. This review introduces several concepts in the design of high-performance gas sensors by analyzing the sensing mechanism of heteronanostructural MOS-based sensors. In addition, the influence of the geometric device structure determined by the interconnection between the sensing materials and the working electrodes is discussed. To systematically investigate the sensing behavior of the sensor, the general sensing mechanism of three typical types of geometric device structures based on different heteronanostructural materials are introduced and discussed in this review. This review will provide guidelines for readers studying the sensing mechanism of gas sensors and designing high-performance gas sensors in the future.

Introduction


Air pollution is becoming a growing concern and a serious worldwide environmental problem that threatens the wellbeing of humans and organisms. Inhalation of gas pollutants can cause many health problems, such as respiratory disease, lung cancer, leukemia, and even early death^{1–4}. It is reported that from 2012 to 2016, millions of people died from air pollution, and billions of people face poor air quality every year⁵. Therefore, it is important to develop portable and miniaturized gas sensors that can provide real-time feedback and high sensing performance

(e.g., sensitivity, selectivity, stability, and response and recovery time). In addition to environmental monitoring, gas sensors also play a crucial role in security^{6–8}, medical diagnosis^{9,10}, aquaculture¹¹, and other fields¹².

To date, several types of portable gas sensors based on different sensing mechanisms, such as optical^{13–18}, electrochemical^{19–22}, and chemiresistive sensors^{23,24}, have been made available. Among them, metal oxide semiconductor (MOS)-based chemiresistive sensors are the most popular in commercial applications due to their high stability and low cost^{25,26}. The concentration of pollutants can be obtained by simply detecting changes in the resistance of MOSs. At the beginning of the 1960s, the first chemiresistive gas sensor based on ZnO film was reported, and it aroused great interest in the field of gas sensing^{27,28}. To date, many different MOSs have been used as gas sensing materials, and they can be divided into two classes according to their physical properties: n-type

Correspondence: Simin Feng (smfeng2020@sinano.ac.cn) or Sujie Qin (Sujie.qin@xjtlu.edu.cn) or Ting Zhang (tzhang2009@sinano.ac.cn)
¹i-Lab, Key Laboratory of Multifunctional Nanomaterials and Smart Systems, Suzhou Institute of Nano-Tech and Nano-Bionics (SINANO), Chinese Academy of Sciences (CAS), Suzhou, Jiangsu, China
²Department of Health and Environmental Sciences, Xi'an Jiaotong-Liverpool University, Suzhou, Jiangsu, China
Full list of author information is available at the end of the article

© The Author(s) 2022

 **Open Access** This article is licensed under a Creative Commons Attribution 4.0 International License, which permits use, sharing, adaptation, distribution and reproduction in any medium or format, as long as you give appropriate credit to the original author(s) and the source, provide a link to the Creative Commons license, and indicate if changes were made. The images or other third party material in this article are included in the article's Creative Commons license, unless indicated otherwise in a credit line to the material. If material is not included in the article's Creative Commons license and your intended use is not permitted by statutory regulation or exceeds the permitted use, you will need to obtain permission directly from the copyright holder. To view a copy of this license, visit <http://creativecommons.org/licenses/by/4.0/>.

MOSs where electrons are the majority charge carriers and p-type MOSs where holes are the majority charge carriers. Normally, p-type MOSs are less popular than n-type MOSs because the sensing response of a p-type MOS (S_p) is proportional to the square root of an n-type MOS ($S_p = \sqrt{S_n}$) under the same presumptions (e.g., same morphological configurations and same band bending changes in the air)^{29,30}. However, the practical applications of single MOS-based sensors still encounter some issues, such as insufficient detection limit and poor sensitivity and selectivity. The selectivity issue can be addressed to some degree by constructing sensor arrays, known as “electronic noses”, and by combining computational analysis algorithms such as learning vector quantization (LVQ), principal component analysis (PCA), and partial least squares (PLS) analysis^{31–35}. In addition, fabrication of low-dimensional MOSs^{32,36–39} (e.g., one-dimensional (1D), 0D and 2D nanomaterials) and modification of backbone MOSs with other nanomaterials (e.g., MOSs^{40–42}, noble metal nanoparticles (NPs)^{43,44}, carbon nanomaterials^{45,46}, and conducting polymers^{47,48}) to construct nanoscale heterojunctions (i.e., heteronanostructural MOSs) are the other preferred approaches to tackle the abovementioned issues. Compared with conventional thick MOS films, low-dimensional MOSs with large specific surface areas could provide more activation sites for gas adsorption and facilitate gas diffusion^{36,37,49}. In addition, the design of MOS-based heteronanostructures can further modulate carrier transport at the heterointerface, leading to larger resistance changes due to the different working functions^{50–52}. Moreover, some chemical effects (e.g., catalytic activity and synergistic surface reactions) originating from designing MOS heteronanostructures could also improve the sensor performance^{50,53,54}. Although the design and construction of MOS-based heteronanostructures would be a promising approach to enhance the sensor performance, current chemiresistive sensors often use a trial-and-error type approach, which is time-consuming and inefficient. Therefore, it is important to understand the sensing mechanism of MOS-based gas sensors, as it can provide a guideline for the directional design of high-performance sensors.

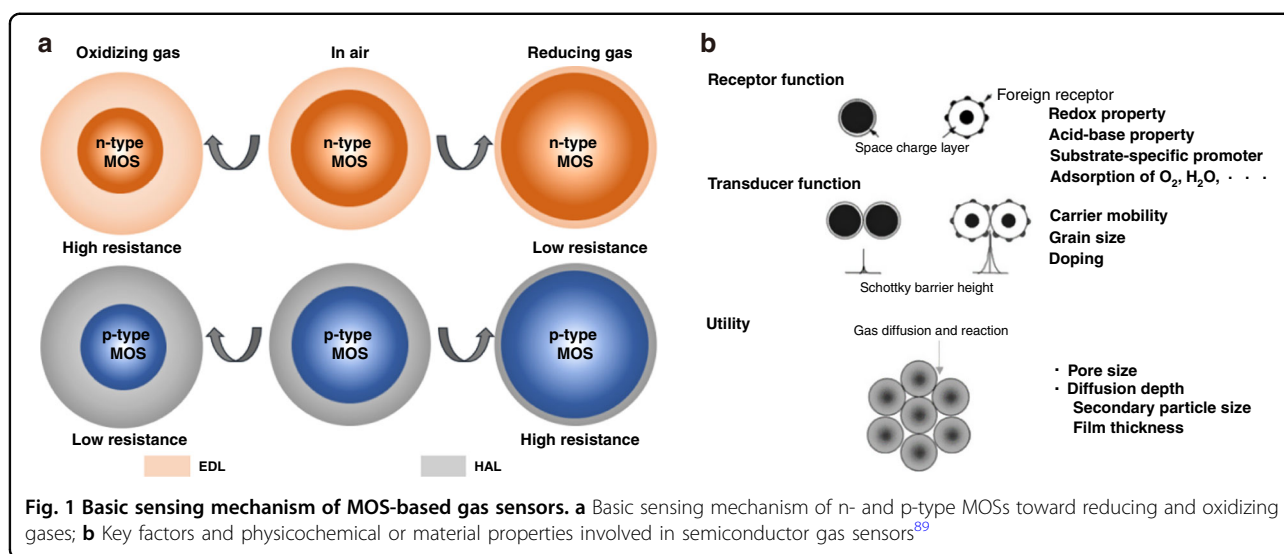
In recent years, MOS-based gas sensors have undergone rapid development, and some review papers about MOS nanostructures^{55–57}, room-temperature gas sensors^{58,59}, specific MOS sensing materials^{60–62}, and specific gas sensors⁶³ have been reported. Other reviews have focused on elucidating the sensing mechanism of gas sensors according to the intrinsic physical and chemical properties of the MOSs, including the role of oxygen vacancies⁶⁴, the role of heteronanostructure^{55,65}, and charge transfer at the heterointerface⁶⁶. Moreover, the sensor performance is also influenced by various other parameters,

including heterostructure, grain size, operation temperature, defect density, oxygen vacancy, and even the exposed crystal facet of the sensing materials^{25,67–73}. However, the geometric device structure determined by the interconnection between the sensing materials and the working electrodes, which is seldom mentioned, can also significantly affect the sensing behavior of the sensor^{74–76} (more details are provided in Section 3). For example, Kumar et al.⁷⁷ reported two gas sensors based on the same materials (e.g., TiO₂@NiO and NiO@TiO₂ bilayer-based gas sensors) and observed different resistance changes upon NH₃ gases due to the different geometric structures of the devices. Therefore, it is important to consider the device structure when analyzing the gas sensing mechanism. In this review, the authors focus on the sensing mechanism based on different heteronanostructures of MOSs and the structures of the devices. We believe that this review could provide guidelines for readers who wish to understand and analyze the gas sensing mechanism, and it may facilitate the design of high-performance gas sensors in the future.

Basic sensing mechanism of a single material and enhancement sensing mechanism of a MOS heterostructure

Figure 1a illustrates the basic gas sensing mechanism model based on a single MOS. When the temperature increases, the adsorption of oxygen molecules (O₂) on the surface of MOS attracts electrons from MOS and form anionic species (such as O²⁻ and O⁻). Then, an electron-depletion layer (EDL) for an n-type MOS or a hole accumulation layer (HAL) for a p-type MOS is formed at the surface of the MOS^{15,23,78}. The interaction between O₂ and MOSs leads to upward bending of the MOS conduction band at the surface and forms a potential barrier. Later, when the sensor is exposed to target gases, the gases adsorbed on the surface of the MOS react with ionic oxygen species by attracting electrons (oxidizing gases) or donating electrons (reducing gases)^{79,80}. The transfer of the electrons between the target gases and MOS can regulate the width of EDL or HAL^{30,81}, resulting in a change in the overall resistance for the MOS-based sensors. For example, for reducing gases, the electrons will transfer from the reducing gases to the n-type MOS, leading to a decrease in EDL and a decrease in resistance, which is named n-type sensing behavior. In contrast, p-type sensing behavior is defined when a p-type MOS is exposed to the reducing gases, HAL will shrink and the resistance will increase due to the donated electrons. For oxidizing gases, the sensor response is opposite to that of reducing gases.

Except for the basic sensing mechanism, the gas sensing mechanisms involved in practical gas sensors are fairly complex. For instance, the practical use of gas sensors



should meet many requirements (*e.g.*, sensitivity, selectivity, and stability) depending on the users' needs. These requirements are closely correlated with the physical and chemical properties of the sensing materials. For example, Xu et al.⁷¹ demonstrated that a SnO_2 -based sensor reached the highest sensitivity when the crystal diameter (d) was comparable to or less than twice the Debye length (λ_D) of SnO_2 ⁷¹. When $d \leq 2\lambda_D$, the SnO_2 is completely depleted after adsorption of O_2 molecules, and the sensing response to the reducing gases is maximized. In addition, various other parameters can also influence the sensor performance, including working temperatures, crystal defects, and even the exposed crystal facets of the sensing materials^{25,67–73}. Specifically, the influence of the working temperatures is ascribed to the possible competition between adsorption and desorption rates of the target gases and the surface reactivity between the adsorbed gas molecules and oxygen species^{4,82}. The effect of crystal defects is greatly related to the content of oxygen vacancies^{83,84}. The sensor performance can also be influenced by the exposed crystal facets due to their different reactivities^{67,85–87}. The exposed crystal facets with lower density reveal more uncoordinated metal cations with higher energy that facilitate surface adsorption and reactivity⁸⁸. Several main factors and relevant enhancement sensing mechanisms are listed in Table 1. Therefore, by tuning these material parameters, the sensing performance can be improved, and it is crucial for determining the key factors that influence the sensor performance.

Yamazoe⁸⁹ and Shimanoe et al.^{68,71} performed many works to study the theoretical sensing mechanism of the sensors and proposed three independent key factors that can affect the performance of the sensors, specifically the receptor function, transducer function, and utility (Fig. 1b). Receptor function means the ability of the MOS

surface to interact with gas molecules. This function is strongly related to the chemical properties of MOS and can be largely improved by introducing foreign receptors (*e.g.*, metal NPs and other MOSs). Transducer function refers to the ability to convert reactions between the gases and MOS surface into electrical signals, and this function is dominated by the grain boundary of MOSs. Therefore, the transducer function is significantly influenced by the grain size of MOSs and the density of foreign receptors. Katoch et al.⁹⁰ reported that reducing the grain size of $ZnO-SnO_2$ nanofibrils leads to the formation of a large number of heterojunctions and improves the sensor sensitivity, which is consistent with the transducer function. Wang et al.⁹¹ compared different Zn_2GeO_4 grain sizes and demonstrated that the sensor sensitivity increased by 6.5 times after grain boundaries were introduced. Utility is another key factor in the performance of the sensors that describes the accessibility of interior MOSs to gases. If the gas molecules cannot access and react with the interior MOSs, the sensor responsivity is reduced. Utility is closely related to the diffusion depth of a specific gas, which is dependent on the pore size of the sensing materials. Sakai et al.⁹² simulated the sensing response of sensors to combustion gases with respect to different diffusion depths of gases inside the sensing films and found that both the molecular weight of the gas and the pore radius of the sensing film can affect the sensor response. Through the above discussions, it is demonstrated that high-performance gas sensors can be designed by balancing and optimizing the receptor function, transducer function and utility⁹³.

The abovementioned works have elucidated the basic sensing mechanism of a single MOS and discussed several factors that impact the MOS performance. In addition to these factors, gas sensors based on heterostructures can

Table 1 Summary of the main factors that influence the sensor performance and relevant enhancement sensing mechanism

Main factors	Materials	Target gases	Response (ppm/ value)	Enhancement sensing mechanism	Ref
Grain size	SnO ₂	Butane	8219.2/8.09 ^c	Smaller grain size induced large specific surface area, increased grain boundaries and volume depletion ($d \sim 2\lambda_d$).	186
	Zeolite/SnO ₂	Formaldehyde	10/11 ^c		187
	ZnO	H ₂ S	0.05/0.142 ^a	188	
	Pd@ZnO	H ₂	10000/~8.5 ^a	170	
	In ₂ O ₃	Formaldehyde	50/~14 ^c	189	
	SnO ₂	H ₂ S	5/13000 ^c	Relative larger grain size in fine grain films (d=0-20 nm) promotes gas diffusion.	68
	Fe ₂ O ₃	Ethanol	100/14.5 ^c	190	
Effects of Heterojunctions	SnO ₂	CO	50/4.5 ^c	191	
	PdO@ZnO	Ethanol	100/35.4 ^c	Heterojunction induces more active site; catalytic effect; modulation of conduction channel and carrier transportation etc.	192
	Fe ₂ O ₃ @NiO	Acetone	100/290 ^b		193
	ZnO-Co ₃ O ₄	Triethylamine	50/67.8 ^c		194
	ZnO-SnO ₂ -RGO	NO ₂	5/141.0 ^d		195
	NiO@SnO ₂	NO ₂	100/~4.4 ^b		196
	SnO ₂ -Co ₃ O ₄	Toluene	1/18.7 ^c		98
CuO-In ₂ O ₃	H ₂ S	5/229.3 ^c	105		
Density of defect	ZnO-Co ₃ O ₄	Ethanol	1000/106 ^b	106	
	ZnO	Acetone	5/~56 ^b	Increased donor defects provide more free electrons for forming active oxygen species.	83
	ZnO	Ethanol	200/193.7 ^b		197
	Co/ZnO	Triethylamine	50/1020 ^c	198	
	ZnO	Ethanol	100/47 ^c	199	
	ZnO	Formaldehyde	200/227.4 ^c	200	
	TiO ₂	H ₂	10/58 ^d	Increased oxygen vacancies provide more oxygen adsorption sites.	201
	Ce-Fe ₂ O ₃	Acetone	100/26.3 ^c		202
	W ₁₈ O ₄₉ @ PANI	NH ₃	100/50 ^b		203
	SnO ₂	H ₂	0.1/1.25 ^c		204
	Mo-SnO ₂	Ethanol	100/46.8 ^b		205
	Tb-SnO ₂	Ethanol	100/53.6 ^c		206
	Sb-SnO ₂ /ZnO	NO ₂	1/9.5 ^a		207
Exposed crystal facet	ZnO	CO	0.45/24.9 ^c	49	
	SnO ₂	Ethanol	100/24.9 ^c	208	
	Bi ₂ MoO ₆	NH ₃	5/53.97 ^b	209	
	In ₂ O ₃	Ethanol	1000/610 ^c	The optimized exposed crystal facet could provide more oxygen vacancies and dangling bonds.	210
	ZnO	Ethanol	50/80 ^c		211
	SnO ₂	Formaldehyde	200/207.7 ^c	212	
	CeO ₂	Dimethylamine	100/142 ^c	87	
Density of defect	Co ₃ O ₄	NO ₂	0.3/0.16 ^d	The optimized exposed crystal facet could provide more lattice oxygen to interact with gases.	213
	SnO ₂	Alkenes	50/40 ^c		214
	Au@SnO ₂	Acetylene	100/77.5 ^b	The optimized exposed crystal facet exhibits higher adsorption energy.	215

a: $(R_g - R_a)/R_a$ b: R_g/R_a c: R_a/R_g d: $(R_g - R_a)/R_a * 100$

further improve the sensor performance by greatly enhancing the transducer function and receptor function⁹³. In addition, heteronanostructures can further improve the sensor performance by enhancing catalytic reactions, modulating charge transport, and providing more adsorption sites⁹⁴. To date, numerous MOS heteronanostructure-based gas sensors have been studied to discuss the enhancement sensing mechanism⁹⁵⁻⁹⁷. Miller et al.⁵⁵ summarized several of the most likely mechanisms responsible for enhancing the sensing performance of heteronanostructures, including surface-

dependent, interface-dependent, and structure-dependent. Among them, the interface-dependent enhancement mechanism is too complicated to cover all interface interactions by one theory, as various heteronanostructural material-based sensors are available (e.g., n-n heterojunctions, p-n heterojunctions, p-p heterojunctions, and Schottky junctions). Generally, sensors based on heteronanostructural MOSs always involve more than two or three enhancement sensing mechanisms⁹⁸⁻¹⁰⁰. The synergistic effects of these enhancement mechanisms can amplify the reception and transduction

of the sensor signal¹⁰¹. Therefore, understanding the sensing mechanism of sensors based on heteronanostructural materials is essential and can guide researchers in the bottom-up design of gas sensors according to their demands. In addition, the geometric device structure can also significantly affect the sensing behavior of the sensor^{74–76}. To systematically analyze the sensing behavior of the sensor, the sensing mechanism of three types of device structures based on different heteronanostructural materials will be introduced and discussed in the following sections.

Three typical device structures and relevant sensing mechanisms

With the rapid development of MOS-based gas sensors, various heteronanostructural MOSs have been proposed. The charge transfer at the heterointerface depends on the different Fermi levels (E_f) of the components. At the heterointerface, the electrons move from one side with higher E_f to the other with lower E_f until their Fermi levels reach equilibrium, and vice versa for holes. Then, the carriers at the heterointerface are depleted and form a depletion layer. Once the sensor is exposed to target gases, the carrier concentration of heteronanostructural MOSs changes, as does the potential barrier height, which amplifies the detection signal. In addition, the various approaches to fabricating heteronanostructures lead to varied interconnections between the materials and electrodes, which produces different geometric device structures and leads to different sensing mechanisms. In this review, we propose three types of geometric device structures and discuss the sensing mechanism of each structure.

Definition of three types of device structures

Although the heterojunction plays a very important role in gas sensing performance, the geometric device structure of the whole sensor can also significantly affect the sensing behavior because the position of the conduction channel of the sensor greatly depends on the geometric device structure. Here, three typical types of geometric device structures based on MOS heterojunctions are discussed and shown in Fig. 2. In the first type, two MOS compounds are randomly distributed between two electrodes, and the position of the conduction channel is determined by the major MOS. In the second type, heteronanostructures are formed from different MOSs, while only one MOS is connected to the electrodes, and the conduction channel is normally located inside one MOS, which is directly connected to the electrodes. In the third type, two materials are connected to the two electrodes separately, and the device is channeled by the formed heterojunction between the two materials.

Sensing Mechanism of the Type-I Sensor Structure

For MOS composite-based gas sensors, two kinds of MOSs are randomly distributed between the electrodes. Many fabrication methods have been developed to obtain MOS composites, including sol-gel, coprecipitation, hydrothermal, electrospinning, and mechanical mixing methods^{98,102–104}. Recently, metal–organic frameworks (MOFs), a class of porous crystalline framework-structured materials, which consist of a metal center and an organic linker, have been used as a template to fabricate porous MOS composites^{105–108}. Notably, even though the composition percentages of MOS composites are the same, the sensing performance can be quite

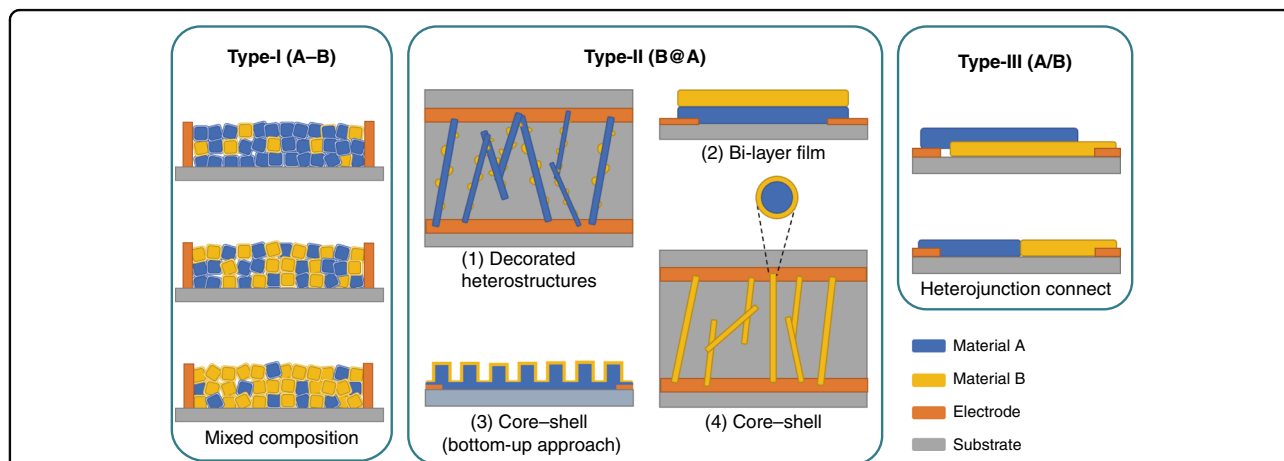


Fig. 2 Three types of device structures. A hyphen between compounds (e.g., “SnO₂-NiO”) indicates that the two constituents are simply mixed (type-I). An “@” between two compounds (e.g., “SnO₂@NiO”) indicates that the backbone material (NiO) is decorated with SnO₂, which is used in the type-II sensor structure. A forward slash (e.g., “NiO/SnO₂”) represents the type-III sensor structure

different when different fabrication processes are used^{109,110}. For instance, Gao et al.¹⁰⁹ prepared two sensors based on MoO₃-SnO₂ composites with the same atomic ratio (Mo:Sn = 1:1.9) and found that different fabrication methods led to different responsivities. Shaposhnik et al.¹¹⁰ reported that the response of coprecipitated SnO₂-TiO₂ to H₂ gases differs from that of the material formed by mechanical mixing, even though the Sn/Ti ratio was the same. This difference occurred because the interconnections between the MOSs and the crystallite size of the MOSs differ with various synthesis methods^{109,110}. When the size and shape of the grains are uniform in terms of donor density and semiconductor type, the response results should remain the same if the contact geometry is unchanged¹¹⁰. Staerz et al.¹¹¹ reported that the sensing performance of SnO₂-Cr₂O₃ core-shell nanofibers (CSNs) and crushed SnO₂-Cr₂O₃ CSNs are practically identical, indicating that the nanofiber morphology shows no advantages if the characteristics of the samples remain unchanged.

In addition to different fabrication methods, the semiconducting type of two different MOSs can also influence the sensing behavior of the sensors. This can be further classified into two categories depending on whether the two MOSs are of the same type of semiconductors (n-n or p-p composite) or different types (p-n composite). When the types of MOS composite-based gas sensors are the same, the sensing response behavior remains unchanged by varying the molar ratio of the two MOSs, while the sensitivity of the sensor changes as the number of n-n or p-p heterojunctions is different¹⁰². When one component dominates in the composites (e.g., 0.9 ZnO-0.1 SnO₂ or 0.1 ZnO-0.9 SnO₂), the conduction channel is determined by the major MOS, which is called the homojunction conduction channel⁹². When the proportion of two components is comparable, the conduction channel is believed to be dominated by the heterojunction^{98,102}. Yamazoe et al.^{112,113} reported that the heterocontact regions of two components could dramatically enhance the sensitivity of the sensor because the heterojunction potential barrier formed due to the different work functions of the components can efficiently tune the drift mobility of electrons when the sensor is exposed to different ambient gases^{112,113}. Figure 3a shows that the sensors based on fibrous SnO₂-ZnO hierarchical structures with different ZnO contents (0 to 10 mol% Zn) can selectively detect ethanol⁵⁴. Among them, the sensor based on the SnO₂-ZnO fiber (7 mol% Zn) exhibited the highest sensitivity due to the formation of a large number of heterojunctions and an increase in the specific surface area, which increased the transducer function and enhanced the sensitivity⁹⁰. However, by further increasing the ZnO component to 10 mol%, the microstructure of the SnO₂-ZnO composites might wrap up the surface

activation sites and reduce the sensing response⁸⁵. A similar tendency can be observed for sensors based on NiO-NiFe₂O₄ p-p heterojunction composites with different Fe/Ni ratios (Fig. 3b)¹¹⁴.

For the case of p-n MOS composites, they exhibit different sensing behaviors depending on the atomic ratio of MOSs¹¹⁵. Generally, the sensing behavior of MOS composites greatly depends on which MOS acts as the dominating conduction channel of the sensor. Therefore, it is very important to characterize the percentage composition and the nanostructure of the composites. Kim et al.⁹⁸ verified this conclusion by synthesizing a series of composite xSnO₂-(1-x)Co₃O₄ nanofibers via an electrospinning method and studying their sensing performance. They observed that the sensing behavior of sensors based on SnO₂-Co₃O₄ composites transits from n-type to p-type sensing behavior by reducing the SnO₂ percentage (Fig. 3c)⁹⁸. Moreover, compared with homojunction-dominated sensors (e.g., SnO₂-rich or Co₃O₄-rich sensors), the heterojunction-dominated sensor (0.5 SnO₂-0.5 Co₃O₄-based) exhibits the highest sensing response to C₆H₆. The intrinsic high resistance of 0.5 SnO₂-0.5 Co₃O₄-based sensor and its higher ability to modulate the total resistance of the sensor contribute to its supreme sensitivity to C₆H₆. Moreover, defects originating from lattice mismatch form at the SnO₂-Co₃O₄ heterointerfaces, which can provide preferential adsorption sites for gas molecules, lead to an enhanced sensing response^{109,116}.

In addition to the semiconducting type of MOSs, the sensing behavior of MOS composites can also be modulated by the chemical properties of the MOS¹¹⁷. Huo et al.¹¹⁷ used a simple soak calcination method to fabricate Co₃O₄-SnO₂ composites and observed that when the Co/Sn molar ratio was 10%, the sensor exhibited a p-type sensing response to H₂, while it demonstrated an n-type sensing response to CO, H₂S, and NH₃ gases, as shown in Fig. 4a¹¹⁷. With a low Co/Sn ratio, many homojunctions form at the SnO₂-SnO₂ nanograin boundaries and exhibit an n-type sensing response to H₂ (Fig. 4b, c)¹¹⁵. By increasing the Co/Sn ratio to 10 mol%, many Co₃O₄-SnO₂ heterojunctions simultaneously form instead of the SnO₂-SnO₂ homojunction (Fig. 4d). Since Co₃O₄ is inactive to H₂ while SnO₂ is highly reactive to H₂, the reaction between H₂ and ionic oxygen species mainly occurs on the surface of SnO₂¹¹⁷. Therefore, the electrons are transferred to SnO₂ and shift the E_f of SnO₂ toward the conduction band, while the E_f of Co₃O₄ remains unchanged. As a result, the resistance of the sensor increases, revealing that the materials with a high Co/Sn ratio exhibit p-type sensing behavior (Fig. 4e). In contrast, CO, H₂S, and NH₃ gases react with ionic oxygen species on both the SnO₂ and Co₃O₄ surfaces, and electrons move from the gases to the sensor, leading to a decrease

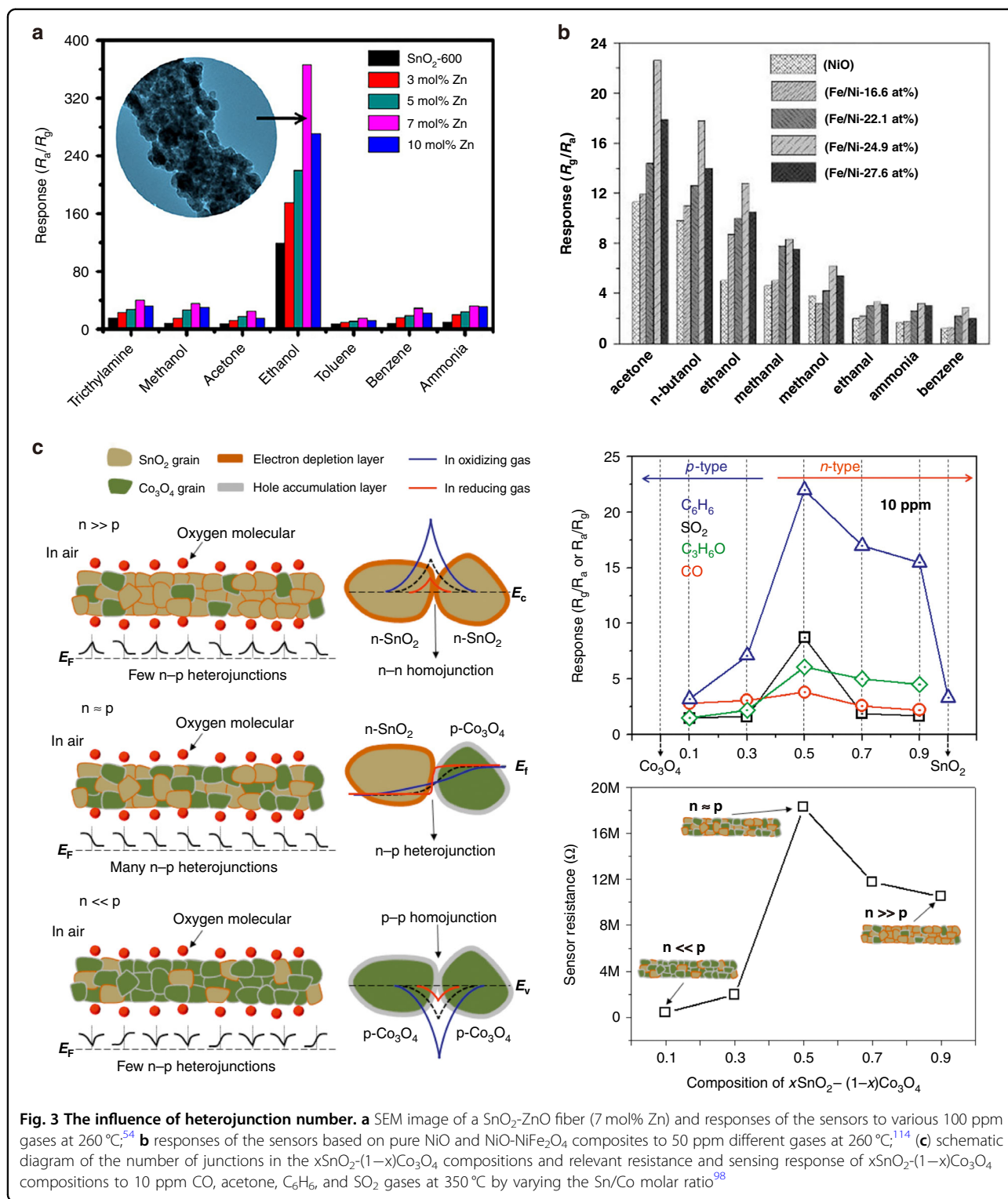
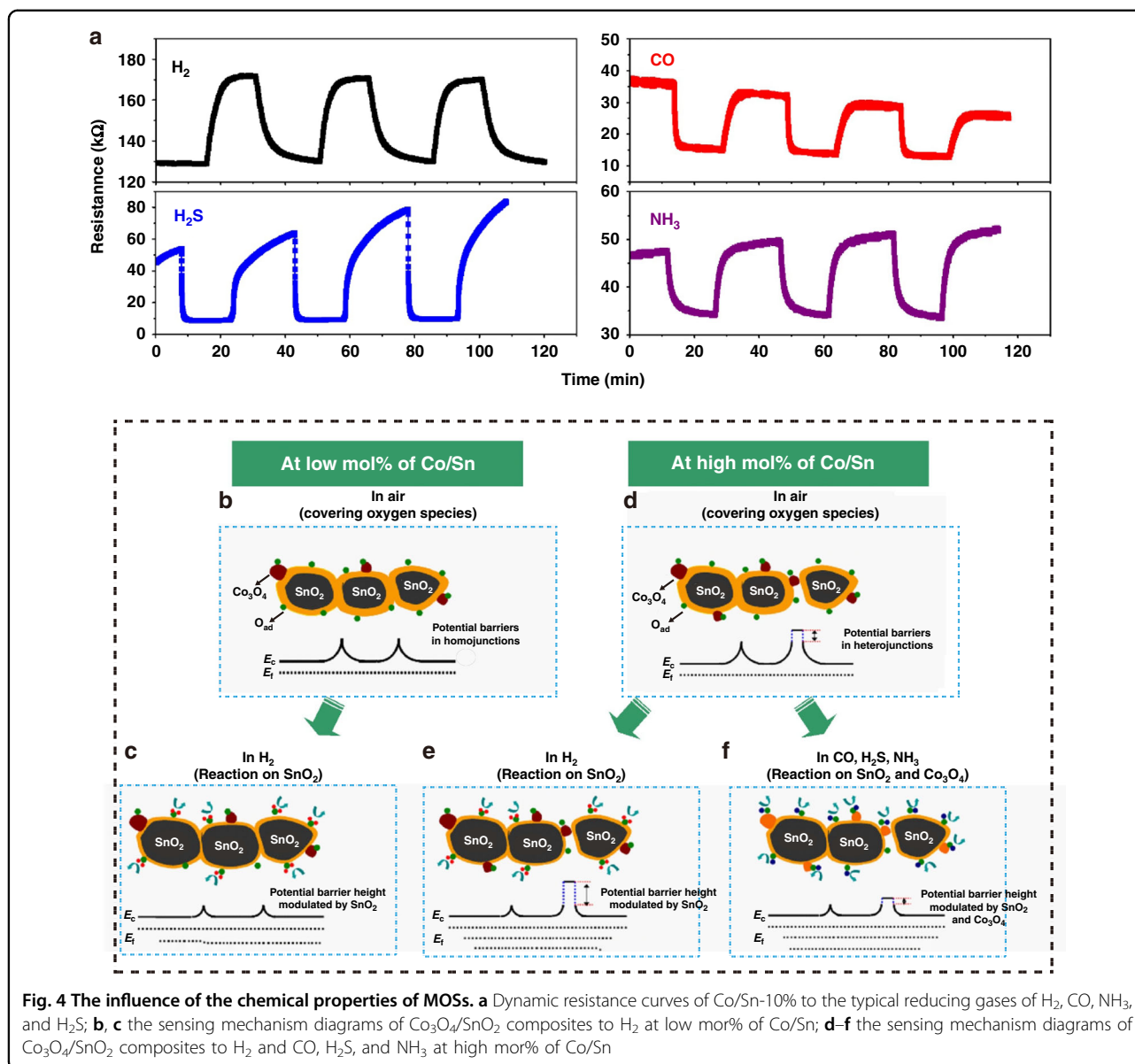


Fig. 3 The influence of heterojunction number. **a** SEM image of a SnO₂-ZnO fiber (7 mol% Zn) and responses of the sensors to various 100 ppm gases at 260 °C;⁵⁴ **b** responses of the sensors based on pure NiO and NiO-NiFe₂O₄ composites to 50 ppm different gases at 260 °C;¹¹⁴ **c** schematic diagram of the number of junctions in the xSnO₂-(1-x)Co₃O₄ compositions and relevant resistance and sensing response of xSnO₂-(1-x)Co₃O₄ compositions to 10 ppm CO, acetone, C₆H₆, and SO₂ gases at 350 °C by varying the Sn/Co molar ratio.⁹⁸

in the potential barrier height and n-type sensing behavior (Fig. 4f). This different sensing behavior is caused by the different reactivity of Co₃O₄ toward various gases and was further verified by Yin et al.¹¹⁸ Similarly, Katoch et al.¹¹⁹ demonstrated that SnO₂-ZnO composites exhibited good

selectivity for H₂ with high sensitivity. This behavior occurs because H atoms can easily adsorb on O sites of ZnO via a strong hybridization between the s-orbitals of H and the p-orbitals of O, which leads to the metallization of ZnO^{120,121}.



In summary, we can enhance the sensitivity of type-I sensors by choosing a proper fabrication method, reducing the grain size of the composites, and optimizing the molar ratio of MOS composites. In addition, a thorough understanding of the chemical properties of the sensing materials can further improve the selectivity of the sensors.

Mechanism of the Type-II Sensor Structure

The type-II sensor structure is another popular sensor structure, and various heteronanostructural materials are available, which consist of one “backbone” nanomaterial and a second or even third nanomaterial. For instance, (1D or 2D materials decorated with nanoparticles, core-shell (C-S), and multilayer heteronanostructure materials

are generally used in type-II sensor structures and will be discussed in detail below.

Decorated heteronanostructures

For the first kind of heteronanostructural material (decorated heteronanostructures), as demonstrated in Fig. 2b (1), the conduction channel of the sensor is connected by the backbone materials. The modified nanoparticles can provide more reaction sites for adsorption or desorption of gases due to the formation of heterojunctions and can also work as catalysts to enhance the sensing performance^{109,122–124}. Yuan et al.⁴¹ observed that decorating WO_3 nanowires with CeO_2 nanodots can provide more adsorption sites at the $CeO_2@WO_3$ heterointerfaces and the CeO_2 surface and generate more chemisorbed

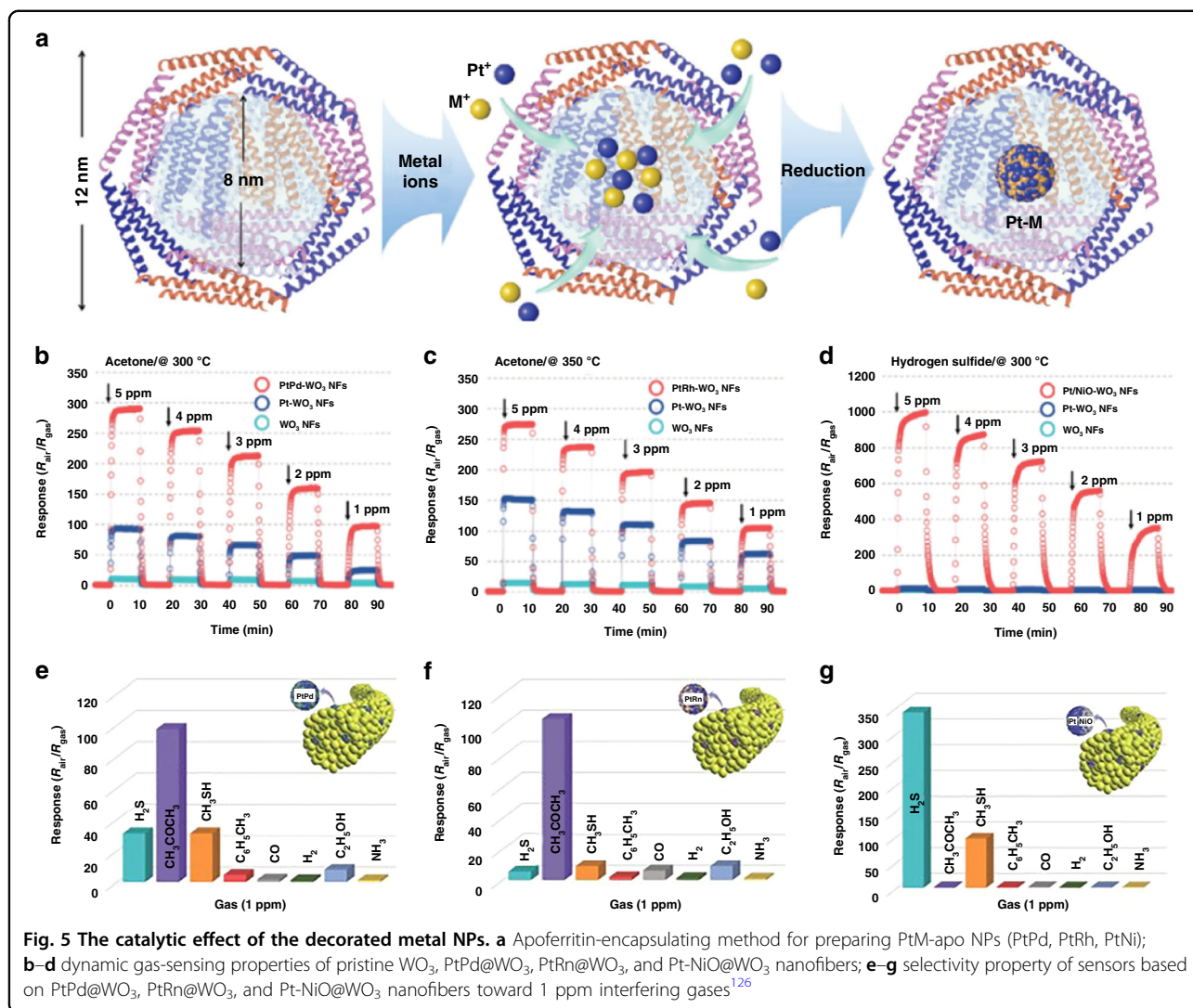
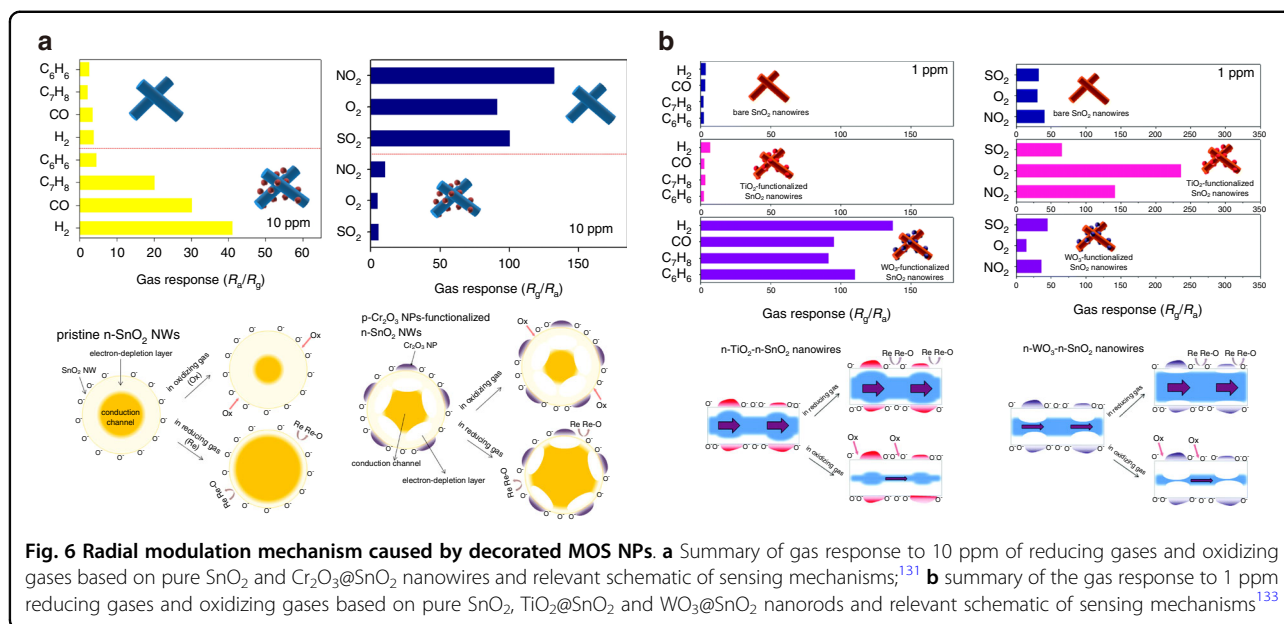


Fig. 5 The catalytic effect of the decorated metal NPs. **a** Apoferritin-encapsulating method for preparing PtM-apo NPs (PtPd, PtRh, PtNi); **b–d** dynamic gas-sensing properties of pristine WO₃, PtPd@WO₃, PtRh@WO₃, and Pt-NiO@WO₃ nanofibers; **e–g** selectivity property of sensors based on PtPd@WO₃, PtRh@WO₃, and Pt-NiO@WO₃ nanofibers toward 1 ppm interfering gases¹²⁶

oxygen species to react with acetone. Gunawan et al.¹²⁵ presented an ultrahigh sensitivity acetone sensor based on 1D Au@ α -Fe₂O₃ and observed that the sensing performance of the sensor is controlled by the activation of O₂ molecules as the oxygen supply. The presence of Au NPs may act as catalysts to promote the dissociation of oxygen molecules into lattice oxygen for the oxidation of acetone¹²⁵. A similar result was observed by Choi et al.⁹ where Pt catalysts were used to dissociate adsorbed oxygen molecules into ionized oxygen species and enhance the sensing response to acetone. In 2017, the same research group demonstrated that the catalytic effect of bimetallic NPs is much higher than that of single noble nanoparticles, as shown in Fig. 5¹²⁶. Figure 5a shows a schematic graph of the fabrication process for Pt-based bimetallic (PtM) NPs with an average size less than 3 nm using an apoferritin protein cage. Then, electrospinning technology was used to obtain PtM@WO₃ nanofibers to improve the sensitivity and selectivity toward acetone or

H₂S (Fig. 5b–g). Recently, owing to maximum atom utilization efficiency and tunable electronic structures, single-atom catalysts (SACs) have exhibited superior catalytic performance in the fields of catalysis and gas sensing^{127,128}. Shin et al.¹²⁹ used Pt SA-anchored shredded melamine-derived carbon nitride nanosheets (MCN), SnCl₂, and PVP as chemical sources to prepare Pt@MCN@SnO₂ fiber-in-tubes for gas sensing. Although the amount of Pt@MCNs was very low (0.13 wt% to 0.68 wt%), Pt@MCN@SnO₂ showed the highest sensing performance toward formaldehyde gas over other reference samples (pristine SnO₂, MCN@SnO₂, and Pt NPs@SnO₂). This superior sensing performance can be explained by the maximized catalyst atom efficiency of Pt SAs and the minimum coverage of the active sites on SnO₂¹²⁹.

In addition, the formed heterojunctions between the backbone material and the nanoparticles can also efficiently modulate the conduction channel via a radial



modulation mechanism to enhance the sensor performance^{130–132}. Figure 6a demonstrates the sensing performance of pure SnO₂ and Cr₂O₃@SnO₂ nanowires to reducing and oxidizing gases and their corresponding sensing mechanisms¹³¹. Compared with pure SnO₂ nanowires, the response of the Cr₂O₃@SnO₂ nanowires to the reducing gases is greatly enhanced, whereas it deteriorates to oxidizing gases. These phenomena are closely related to the local suppression of the conduction channel of SnO₂ nanowires in the radial direction of the formed p-n heterojunction¹³¹. The resistance of the sensor is simply tuned by changing the width of the EDL on the surface of the pure SnO₂ nanowires after exposure to the reducing and oxidizing gases¹³¹. However, for Cr₂O₃@SnO₂ nanowires, the initial EDL of the SnO₂ nanowires in the air is expanded, and the conduction channel is suppressed compared with that of the pure SnO₂ nanowires due to the formed heterojunctions. Therefore, when the sensor is exposed to reducing gases, captured electrons are released to the SnO₂ nanowires, and the EDL dramatically shrinks, resulting in a higher sensitivity than that of the pure SnO₂ nanowires. In contrast, when switching to oxidizing gases, the expansion of the EDL is limited, which leads to low sensitivity. Similar sensing response results were observed by Choi et al.¹³³, where the sensing response of SnO₂ nanowires decorated with p-type WO₃ nanoparticles for reducing gases was significantly improved, while an enhanced sensitivity to oxidizing gases was observed for a SnO₂ sensor decorated with n-type TiO₂ nanoparticles (Fig. 6b)¹³³. This result was mainly due to the different working functions between the SnO₂ and MOS nanoparticles (TiO₂ or WO₃). In p-type (n-type) nanoparticles, the

conduction channel of the backbone material (SnO₂) expands (or shrinks) radially, and then further expansion (or shortening) of the SnO₂ conduction channel is marginal upon exposure to reducing (or oxidizing) gases (Fig. 6b).

Bilayer and multilayer heteronanostructures

In bilayer and multilayer heteronanostructure devices, the conduction channel of the device is dominated by the layer that is directly in contact with the electrodes (generally the bottom layer), and the heterojunctions formed at the contact regions of the two layers can modulate the conductance of the bottom layer. Therefore, once the gases interact with the top layer, they significantly influence the conduction channel of the bottom layer and the resistance of the device¹³⁴. For instance, Kumar et al.⁷⁷ reported the opposite sensing behavior of TiO₂@NiO and NiO@TiO₂ bilayer films toward NH₃. This discrepancy occurs because the conduction channels of the two sensors are dominant in different material layers (NiO and TiO₂, respectively), and then the changes in the conduction channel in the bottom layer are different⁷⁷.

Bilayer or multilayer heteronanostructures are commonly obtained by sputtering, atomic layer deposition (ALD), and spin coating^{56,70,134–136}. The thicknesses of the films and the contact areas of the two materials can be well controlled. Figure 7a and b show the NiO@SnO₂ and Ga₂O₃@WO₃ nanofilms prepared by the sputtering method for ethanol sensing^{135,137}. However, these methods usually result in planar films, and the sensitivity of these planar films is lower than that of 3D nanostructured materials due to their low specific surface area and low gas permeation rate. Thus, liquid phase strategies have also

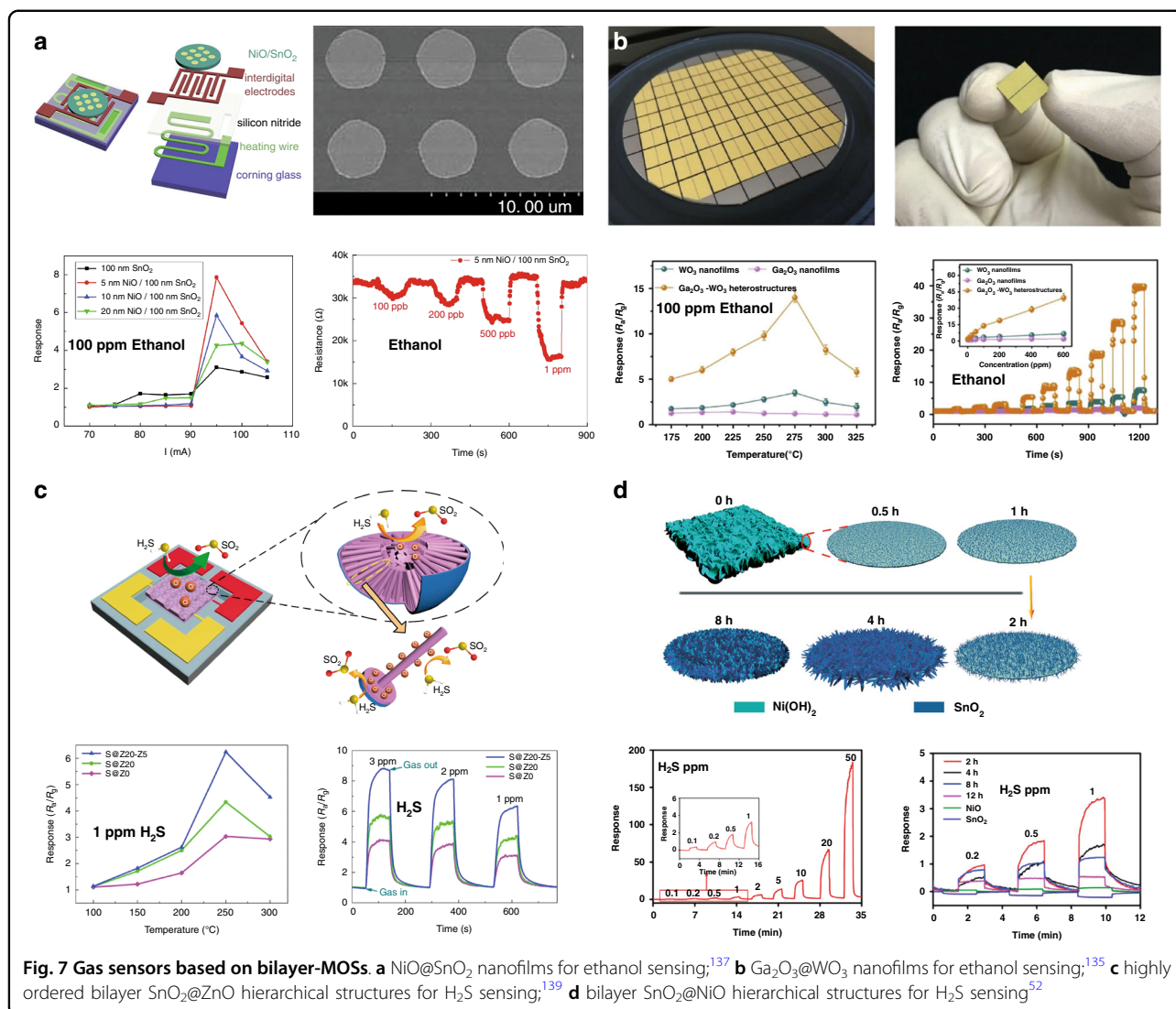


Fig. 7 Gas sensors based on bilayer-MOSs. **a** NiO@SnO₂ nanofilms for ethanol sensing;¹³⁷ **b** Ga₂O₃@WO₃ nanofilms for ethanol sensing;¹³⁵ **c** highly ordered bilayer SnO₂@ZnO hierarchical structures for H₂S sensing;¹³⁹ **d** bilayer SnO₂@NiO hierarchical structures for H₂S sensing⁵²

been proposed to fabricate bilayer films with different hierarchical structures to increase the sensing performance by increasing the specific surface area^{41,52,138}. Zhu et al.¹³⁹ combined sputtering and hydrothermal methods and obtained highly ordered ZnO nanowires on top of SnO₂ nanobowls (ZnO@SnO₂ nanowires) for H₂S sensing (Fig. 7c). Its responsivity to 1 ppm H₂S is 1.6-fold higher than that of sensors based on the ZnO@SnO₂ nanofilm, which is prepared by sputtering. Liu et al.⁵² reported a high-performance H₂S sensor by fabricating SnO₂@NiO hierarchical nanostructures with an in-situ two-step chemical bath deposition method followed by thermal annealing treatment (Fig. 10d). Compared with conventional SnO₂@NiO bilayer films, which are prepared by the sputtering method, the sensing performance of the hierarchical SnO₂@NiO bilayer structure is dramatically enhanced owing to the increase in the specific surface area^{52,137}.

Core-shell heteronanostructures

In core-shell heteronanostructure (CSHN)-based type-II devices, the sensing mechanism is more complex since the conduction channel is not confined to the inner shell. The fabrication routes and the thicknesses of the shell (t_s) can both determine the location of the conduction channel. For example, the conduction channel is normally confined to the inner core when using bottom-up synthesis approaches, and the structure is similar to bilayer or multilayer device structures (Fig. 2b(3))^{123,140–143}. Xu et al.¹⁴⁴ reported a bottom-up approach to prepare NiO@ α -Fe₂O₃ and CuO@ α -Fe₂O₃ CSHNs by depositing a layer of NiO or CuO NPs on top of α -Fe₂O₃ nanorods, in which the conduction channel is confined to the core part (α -Fe₂O₃ nanorods). Liu et al.¹⁴² also successfully confined the conduction channel to the core part of TiO₂@Si CSHNs by drop-casting TiO₂ onto the as-prepared Si nanowire array. Therefore, its sensing

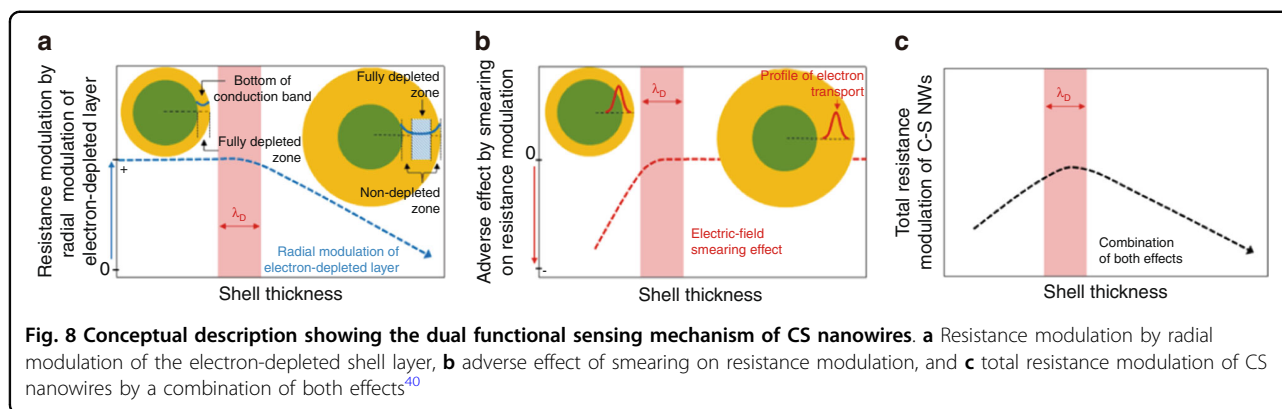


Fig. 8 Conceptual description showing the dual functional sensing mechanism of CS nanowires. **a** Resistance modulation by radial modulation of the electron-depleted shell layer, **b** adverse effect of smearing on resistance modulation, and **c** total resistance modulation of CS nanowires by a combination of both effects⁴⁰

behavior (p-type or n-type) only depends on the semi-conducting type of Si nanowires.

However, most reported CSHN-based sensors (Fig. 2b(4)) are prepared by transferring synthesized CS material powders onto a chip. In this case, the conduction channel of the sensor is influenced by the thickness of the shell (h_s). Kim's group studied the effects of h_s on the gas sensing performance and proposed a possible sensing mechanism^{100,112,145–148}. It is believed that two factors contribute to the sensing mechanism of this structure: (1) the radial modulation of the EDL of the shell and (2) the electric field smearing effect (Fig. 8)¹⁴⁵. The researchers mentioned that the conduction channel of the carriers is mostly confined to the shell layer when $h_s > \lambda_D$ of the shell layer¹⁴⁵. As a result, the resistance modulation of sensors based on CSHNs is mainly dominated by the radial modulation of the EDL of the shell (Fig. 8a). However, when $h_s \leq \lambda_D$ of the shell layer, the shell layer becomes fully electron depleted by the adsorbed oxygen species and the formed heterojunction at the CS heterointerface. Therefore, the conduction channel is not only located inside the shell layer but also partially in the core part, especially when $h_s < \lambda_D$ of the shell layer. In this case, both the fully electron-depleted shell layer and the partially depleted core layer contribute to modulating the resistance of the whole CSHNs, generating an electric-field smearing effect (Fig. 8b). Some other studies use the concept of EDL volume fraction instead of electric field smearing effect to analyze the effect of h_s ^{100,148}. By taking both contributions into consideration, the overall resistance modulation of the CSHNs reaches the highest when h_s is comparable with λ_D of the shell layer, as shown in Fig. 8c. Therefore, the optimal h_s of the CSHN may be close to λ_D of the shell layer, which is consistent with experimental observations^{99,144–146,149}. Several studies have demonstrated that h_s can also influence the sensing behavior of sensors based on p-n heterojunction CSHNs^{40,148}. Lee et al.¹⁴⁸ and Bai et al.⁴⁰ systematically studied the influence of h_s on the performance of p-n heterojunction CSHN (e.g., TiO₂@CuO and ZnO@NiO)-

based sensors by varying the ALD cycles of the shell layer. As a result, the sensing behavior transits from p-type to n-type with increasing h_s ^{40,148}. This behavior occurs because at the beginning (with a limited ALD cycle number), the heterostructure can be regarded as decorated heteronanostructures. Thus, the conduction channel is confined to the core layer (p-type MOS), and the sensor shows p-type sensing behavior⁴⁰. By increasing the ALD cycle number, the shell layer (n-type MOS) becomes quasi-continuous and serves as the conduction channel, resulting in n-type sensing behavior⁴⁰. Similar sensing transition behaviors have also been reported on branched p-n heteronanostructures^{150,151}. Zhou et al.¹⁵⁰ studied the sensing behavior of Zn₂SnO₄@Mn₃O₄ branched heteronanostructures by tuning the content of Zn₂SnO₄ on the surface of Mn₃O₄ nanowires. The p-type sensing behavior is observed when Zn₂SnO₄ seeds form on the surface of Mn₃O₄. With a further increase in the content of Zn₂SnO₄, the sensor based on Zn₂SnO₄@Mn₃O₄ branched heteronanostructures switches to n-type sensing behavior.

In summary, the type-II sensor involves many different hierarchical nanostructures, and the sensor performance depends largely on the position of the conduction channel. Therefore, it is crucial to control the location of the conduction channel of the sensor and use a suitable model based on heteronanostructural MOSs to study the enhanced sensing mechanism of the type-II sensor.

Sensing mechanism of the type-III sensor structure

The type-III sensor structure is not very common, and the conduction channel is based on the formed heterojunction between the two semiconductors, which are separately connected to the two electrodes. The unique device structure is usually obtained via microfabrication techniques, and the sensing mechanism is quite different from those of the previous two types of sensor structures. The I - V curves of the type-III sensor usually present the typical rectification characteristics due to the formed heterojunctions^{48,152,153}. The I - V curves of the ideal

heterojunction could be described by the thermionic emission mechanism of electrons over the heterojunction barrier height^{152,154,155}.

$$I = I_S \left[\exp\left(\frac{qV_a}{kT}\right) - 1 \right] = A(J_n + J_p) \quad (1)$$

where V_a is the bias voltage, A is the device area, k is the Boltzmann constant, T is the absolute temperature, q is the electrical charge of the carrier, and J_n and J_p represent the hole and electron diffusion current densities, respectively. I_S represents the reverse saturation current given by the following equation:^{152,154,155}

$$I_S = AA^* T^2 \exp\left(\frac{-qV_{bi}^0}{kT}\right) \quad (2)$$

where A^* is the Richardson constant and V_{bi}^0 is the built-in potential.

Therefore, the total current of the p-n heterojunction is determined by both the changes in the carrier concentrations and the heterojunction barrier height, as illustrated by Eqs. (3) and (4)¹⁵⁶

$$J_p = \frac{qD_p}{L_p} p_{p0} \exp\left(\frac{-qV_{bi}^0}{kT}\right) \exp\left(\frac{-\Delta E_v}{kT}\right) \left[\exp\left(\frac{qV_a}{kT}\right) - 1 \right] \quad (3)$$

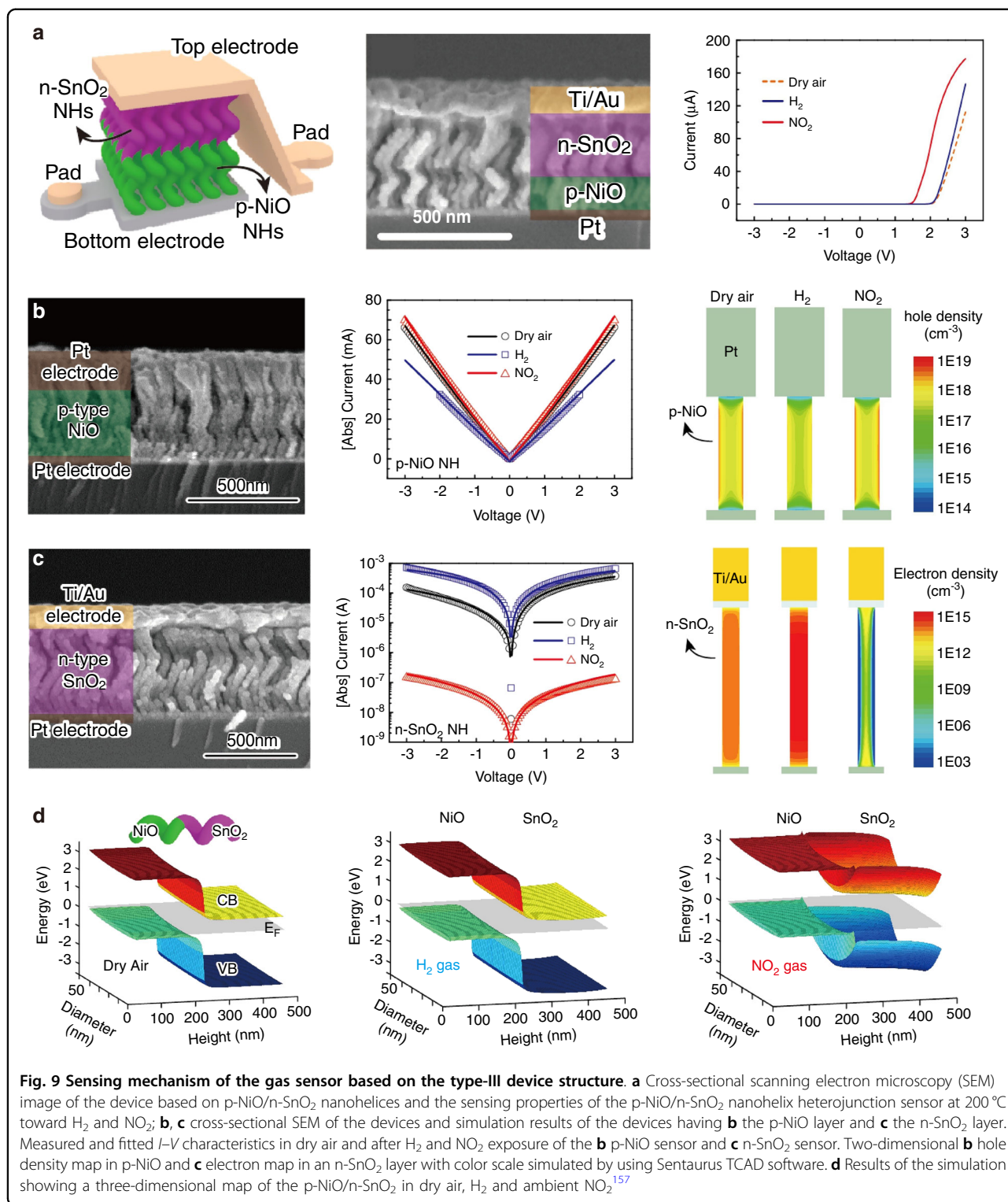
$$J_n = \frac{qD_n}{L_n} n_{n0} \exp\left(\frac{-qV_{bi}^0}{kT}\right) \exp\left(\frac{-\Delta E_c}{kT}\right) \left[\exp\left(\frac{qV_a}{kT}\right) - 1 \right] \quad (4)$$

where n_{n0} and p_{p0} are the electron (hole) concentrations in n-type (p-type) MOSs, V_{bi}^0 is the built-in potential, D_p (D_n) is the diffusion coefficient for the electron (hole), L_n (L_p) is the diffusion length for the electron (hole), and ΔE_v (ΔE_c) is the energy shift of the valence band (conduction band) at the heterointerface. Although the current density is proportional to the carrier density, it is inversely exponentially correlated with V_{bi}^0 . Therefore, the overall change in the current density is significantly dependent on the modulation of the heterojunction barrier height.

As discussed above, the construction of hetero-nanostructural MOS (e.g., type-I and type-II devices) can dramatically enhance the sensor performance over that of the individual components. Whereas, for the type-III device, the response of hetero-nanostructure can be either higher than both the components^{48,153} or just higher than only one component⁷⁶ depending on the chemical properties of the materials. Several reports have illustrated that when one of the components is insensitive to target gases, the response of the hetero-nanostructure is much higher than that of individual components^{48,75,76,153}. In this case, the target gas would just interact with the sensitive layer and cause the shift of E_f for the sensitive layer as well as

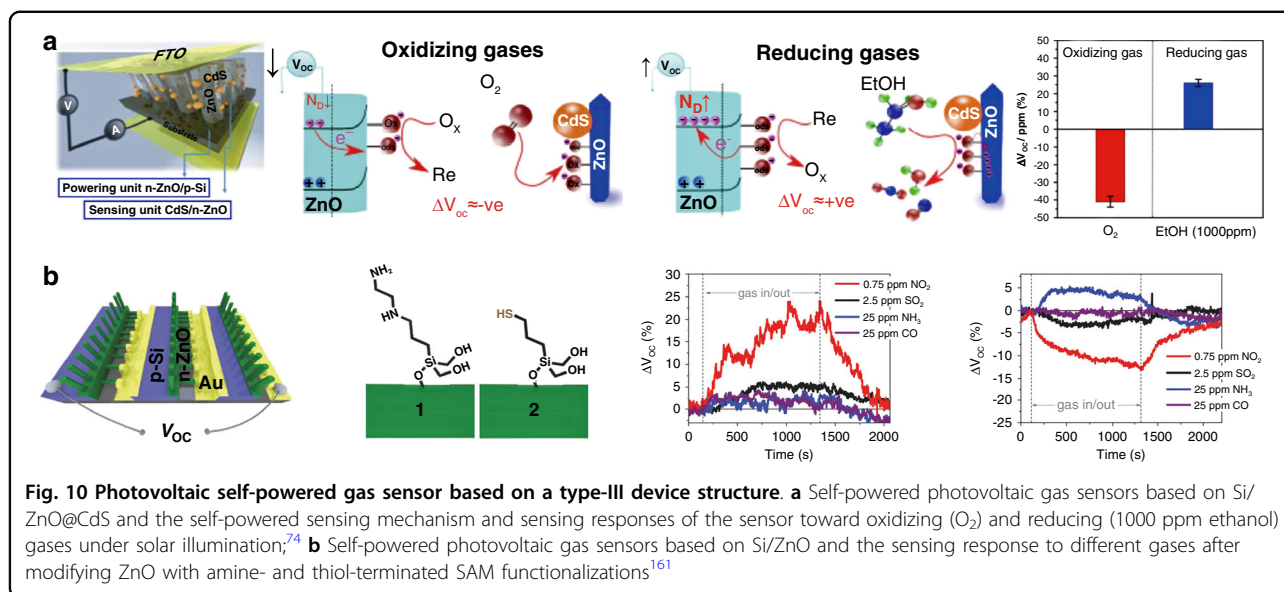
the change of heterojunction barrier height¹⁴⁷. Then, the total current of the device dramatically changes as it is inverse exponentially correlated with the heterojunction barrier height according to Eqs. (3) and (4)^{48,76,153}. However, when both n-type and p-type components are sensitive to target gases, the sensing performance may lie in between. Jose et al.⁷⁶ used the sputtering method to obtain a NiO/SnO₂ porous thin film-based NO₂ sensor and found that the sensitivity of the sensor was only higher than that of a NiO-based sensor but lower than that of a SnO₂-based sensor. This phenomenon is because SnO₂ and NiO exhibit opposite responses to NO₂⁷⁶. In addition, as the two components show different sensitivities to gases, they may cause the same trend in sensing oxidizing and reducing gases. For instance, Kwon et al.¹⁵⁷ proposed a NiO/SnO₂ p-n heterojunction-based gas sensor via an oblique-angle deposition method, as shown in Fig. 9a. Interestingly, the sensor based on the NiO/SnO₂ p-n heterojunction showed the same sensing trend to H₂ and NO₂ (Fig. 9a). To address this result, Kwon et al.¹⁵⁷ systematically studied how NO₂ and H₂ would change the carrier concentration and modulate the V_{bi}^0 of both materials via I-V characterization and computational simulation (Fig. 9 b–d). Figure 9b, c demonstrate the ability of H₂ and NO₂ to change the carrier density of the sensor based on p-NiO (p_{p0}) and n-SnO₂ (n_{n0}), respectively. They show that the p_{p0} of p-type NiO changed slightly in the NO₂ environment, while a dramatic change occurred in the H₂ environment (Fig. 9b). However, n_{n0} showed the opposite behavior for n-type SnO₂ (Fig. 9c). Based on these results, the authors concluded that when the sensor based on the NiO/SnO₂ p-n heterojunction was exposed to H₂, the increase in n_{n0} led to an increase in J_n and the slight increase in V_{bi}^0 led to a low response (Fig. 9d). After exposure to NO₂, the large decrease in n_{n0} in SnO₂ and the small increase in p_{p0} in NiO both led to a large decrease in V_{bi}^0 , which ensured an enhancement of the sensing response (Fig. 9d)¹⁵⁷. In summary, both changes in the carrier concentrations and V_{bi}^0 can lead to the variation of the total current, which further influences the sensing capability.

In addition to the chemical properties of the materials themselves, the Type-III device structure shows the ability to construct a self-powered gas sensor, which cannot be achieved by type-I and type-II devices. The p-n heterojunction diode structure is commonly utilized to construct photovoltaic devices owing to the inherent electric field (BEF) and shows the potential to fabricate photovoltaic room temperature self-powered gas sensors under light illumination^{74,158–161}. The BEF at the heterointerface, which results from the difference in Fermi levels of the materials, can also contribute to the separation of electron-hole pairs. The merit of the photovoltaic self-powered gas sensor lies in its low energy consumption, as



it can absorb energy from illuminated light and then drive itself or other miniaturized devices without external energy sources. For instance, Tanuma and Sugiyama¹⁶² fabricated a NiO/ZnO p-n heterojunction as a solar cell to activate a polycrystalline SnO₂-based CO₂ sensor. Gad

et al.⁷⁴ reported a photovoltaic self-powered gas sensor based on a Si/ZnO@CdS p-n heterojunction, as demonstrated in Fig. 10a. Vertically aligned ZnO nanowires were directly grown on the p-type Si substrate to form a Si/ZnO p-n heterojunction. Then, CdS nanoparticles were



decorated on the surface of ZnO nanowires via chemical surface modification. Figure 10a demonstrates the sensing response results of Si/ZnO@CdS to O₂ and ethanol under self-powered mode. Under light illumination, the open-circuit voltage (V_{oc}), which was induced by the separation of electron-hole pairs under the BEF at the heterointerface of Si/ZnO, increased linearly with the number of connected diodes^{74,161}. V_{oc} can be expressed by Eq. (5)¹⁵⁶,

$$V_{oc} = \frac{kT}{q} \ln \left(\frac{N_D^{ZnO} N_A^{Si}}{N_i^{ZnO} N_i^{Si}} \right) \quad (5)$$

where N_D , N_A , and N_i are the concentrations of the donor, acceptor, and intrinsic carrier, respectively, and k , T , and q represent the same parameters as in previous equations. When exposure to oxidizing gases, they withdraw electrons from the ZnO nanowires and result in a decrease in N_D^{ZnO} and then V_{oc} . In contrast, the reducing gases lead to an increase in V_{oc} (Fig. 10a). By decorating ZnO with CdS nanoparticles, the photoexcited electrons in the CdS nanoparticles are injected into the conduction band of ZnO and interact with adsorbed gases, resulting in improved sensing performance^{74,160}. Hoffmann et al.^{160,161} reported a similar photovoltaic self-powered gas sensor based on Si/ZnO (Fig. 10b). The sensor can selectively detect NO₂ by modulating the working function of target gases by functionalizing ZnO nanowires with amine ([3-(2-aminoethylamino) propyl] trimethoxysilane) (amine functionalized-SAM) and thiol ((3-mercapto-propyl)-trimethoxysilane) (thiol functionalized-SAM)) (Fig. 10b)^{74,161}.

Therefore, when discussing the sensing mechanism of type-III sensors, it is very important to determine the changes in the heterojunction barrier height and the

ability of gases to affect carrier concentrations. In addition, light illumination can produce photogenerated carriers that react with gases, and these carriers are promising for self-powered gas detection.

Conclusions, future outlook, remaining challenges

As discussed in this literature review, many different MOS heteronanostructures have been fabricated to enhance the performance of sensors. Various keywords (metal oxide composites, core-shell metal oxide, hierarchical metal oxide, and self-powered gas sensor) were searched on the Web of Science database, and the differentiating features (popularity, sensitivity/selectivity, power generation potential, fabrication method, and conduction channel) of the three types of devices are summarized in Table 2. A general concept of how to design high-performance gas sensors has been discussed by analyzing the three key factors proposed by Yamazoe. Researchers have further discussed and classified the enhancement sensing mechanisms of sensors based on MOS heteronanostructures. To understand the influencing factors of gas sensors, various parameters of MOSs (e.g., grain size, operation temperatures, density of defects and oxygen vacancies, exposed crystal facet) have been investigated thoroughly. However, the influence of the geometric device structure, which is also critical to the sensing behavior of the sensors, has been ignored and has seldom been discussed. In this review, the basic sensing mechanisms of three typical types of device structures are discussed.

The grain size structure, fabrication method, and number of heterojunctions formed by the sensing materials in type-I sensors can greatly influence the sensitivity of the sensors. In addition, the sensing behavior is also

Table 2 Comparison of the features of three device structures

Sensor type	Popularity	Sensitivity	Selectivity	Power generation potential	Main fabrication method	Conduction channel
Type-I	g	g	g	p	sol-gel; coprecipitation; hydrothermal; electrospinning; mechanical mixing	Determined by the major MOS
Type-II	e	e	g	p	hydrothermal; sputtering; ALD; spin coating	Normally it is located in the MOS, which is connected with two electrodes; it may also be located in the core layer of the CS structure.
Type-III	p	p	p	e	sputtering; hydrothermal	Channeled by the formed heterojunction

where e means excellent, g means good, and p means poor

influenced by the molar ratio of the components. The type-II device structure (decorated heteronanostructures, bilayer or multilayer films, and CSHNs) is the most popular device structure; it consists of two or more components, and only one of them connects to the electrodes. For this device structure, it is critical to determine the location of the conduction channel and its relative changes when studying the sensing mechanism. As type-II devices involve many different hierarchical heteronanostructures, many different sensing mechanisms have been proposed. In the type-III sensor structure, the conduction channel is dominated by the formed heterojunction at the heterointerface, and the sensing mechanism is quite different. Therefore, it is very important to determine the changes in the heterojunction barrier height of the type-III sensors once exposed to target gases. With this structure, it is possible to fabricate photovoltaic self-powered gas sensors to reduce power consumption. However, there is much progress to be made in studies of self-powered gas sensors since their current fabrication process is rather complicated and the sensitivity is much lower than that of traditional MOS-based chemiresistive gas sensors.

The key advantages of MOS gas sensors with hierarchical heteronanostructures are their fast responses and improved sensitivity. However, several key challenges (*e.g.*, high working temperature, long-term stability, poor selectivity and reproducibility, humidity impact, and so on) of MOS gas sensors remain and need to be addressed before they can be used in practical applications. Current MOS gas sensors usually work under high temperatures, which causes high power consumption and impacts the long-term stability of sensors. There are two common approaches to address this problem: (1) the design of low power consumption sensor chips and (2) the development

of novel sensing materials that can work at low temperatures or even at room temperature. One method of designing low power consumption sensor chips, one of the method is to minimize the sensor size by fabricating ceramic-based and silicon-based microhotplates¹⁶³. The power consumption of ceramic-based microhotplates is approximately 50–70 mW per sensor, while the power consumption of optimized silicon-based microhotplates can decrease to 2 mW per sensor when operated continuously at 300 °C^{163,164}. The development of novel sensing materials is an effective way to reduce the power consumption by decreasing the working temperature and can also improve the stability of the sensor. The thermal stability of MOSs becomes more challenging when the size of MOSs continues to reduce to improve the sensor sensitivity, which results in the signal drift of the sensor¹⁶⁵. In addition, high temperature promotes the diffusion of materials across the heterointerfaces and form mixed phases, which affects the electronic properties of sensors¹⁶⁶. Researchers have reported that the optimized operation temperatures of sensors can be reduced by choosing appropriate sensing materials and designing MOS heteronanostructures^{167,168}. Seeking a low-temperature method of fabricating highly crystalline MOS heteronanostructures is another promising approach to enhancing stability¹⁶⁸.

The selectivity of MOS-based sensors is another practical issue because various gases coexist with the target gas, and MOS-based sensors are normally sensitive to more than one gas and usually show cross-sensitivities. Therefore, it is crucial to improve the selectivity of the sensor to a target gas among other gases for real-world applications. Over the past few decades, the selectivity has been partially addressed by constructing gas sensor arrays known as “electronic noses (E-noses)”, and combining computational analysis

algorithms such as learning vector quantization (LVQ), principal component analysis (PCA), partial least squares (PLS), and so on^{31–34}. Two main factors (the number of sensors, which is greatly related to the kinds of sensing materials, and the computational analysis) are essential for enhancing the ability of the E-nose to distinguish gases¹⁶⁹. However, it usually requires many complex fabrication processes to increase the sensor number; thus, it is crucial to seek a facile method to enhance the E-nose performance. In addition, modification of the MOS with other materials can also enhance the selectivity of the sensor. For example, one can realize the selective detection of H₂ using Pd NP-decorated MOSs due to their good catalytic activity¹⁷⁰. In recent years, some researchers have covered the surface of MOSs with MOFs to improve the sensor selectivity through the size-exclusive effect^{171,172}. Inspired by this work, the functionalization of materials may address the issue of selectivity in some way. However, much work still needs to be performed on how to choose appropriate materials.

Reproducibility in performance among sensors fabricated under identical conditions and methods is another important requirement of large-scale fabrication and practical applications. Generally, spin- and dip-coating methods are low-cost routes to fabricate gas sensors with high throughput. However, during these processes, the sensing materials tend to aggregate, and the interconnections between the sensing materials and the substrates are weak^{68,138,168}. Therefore, the sensitivity and stability of the sensors are significantly influenced, and the performance reproducibility is poor. Other fabrication methods, such as sputtering, ALD, pulsed laser deposition (PLD) and physical vapor deposition (PVD), can directly yield bilayer or multilayer MOS films on patterned silicon or alumina substrates. These techniques can avoid aggregation of the sensing materials and ensure the reproducibility of the sensors and demonstrate the feasibility for large-scale fabrication of planar film-based sensors¹⁷³. However, the sensitivity of these planar films is usually much lower than that of 3D nanostructured materials due to their low specific surface area and low gas permeation rate^{41,174}. New strategies for growing MOS heteronanostructures at specific locations on patterned microchips and precisely controlling the size, thickness and morphology of the sensing materials are essential for the low-cost wafer-scale fabrication of sensors with high reproducibility and sensitivity. For instance, Liu et al.¹⁷⁴ proposed a combined “top-down” and “bottom-up” strategy to manufacture wafer-scale miniaturized gas sensors with high throughput by in-situ growth of Ni(OH)₂ nanowalls at specific locations of the microhotplate wafer.

In addition, it is important to consider the impact of humidity on the sensor in real-world applications. The water molecules can compete with oxygen molecules for the adsorption site of the sensing materials and influence

the responsibility of the sensors to target gases¹⁷⁵. Similar to oxygen gases, water acts as a molecule via physical adsorption and can also present as hydroxyl radicals or hydroxyl groups in multiple oxidation stations via chemical adsorption¹⁷⁶. Furthermore, the reliable response of sensors to target gases is a great challenge due to the high level and nonconstant humidity in the environment. Several strategies have been developed to address this issue, such as the gas preconcentration method¹⁷⁷, humidity compensation and cross-reactive array method¹⁷⁸ and dehumidification techniques^{179,180}. However, these methods are costly and complex and lower the sensor's sensitivity. Some low-cost strategies have been proposed to suppress the impact of humidity. For example, decorating SnO₂ with Pd NPs can facilitate the transition of adsorbed oxygen into anionic species, and functionalization of SnO₂ with materials (*e.g.*, NiO and CuO) with a high affinity to water molecules are two possible methods to prevent the humidity dependence of the sensors^{181–183}. In addition, the construction of hydrophobic surfaces by introducing hydrophobic materials can also reduce the influence of humidity^{36,138,184,185}. However, the design of humidity-resistant gas sensors remains in its early stage, and more advanced strategies are needed to tackle these problems.

In conclusion, improvements in sensing performance (*e.g.*, sensitivity, selectivity, low optimal working temperature) have been achieved by the construction of MOS heteronanostructures, and different enhancement sensing mechanisms have been proposed. The geometric device structure must also be taken into consideration when studying the sensing mechanism of a specific sensor. To further improve the performance of gas sensors and address the remaining challenges, exploring novel sensing materials and investigating advanced fabrication strategies are needed in the future. To tune the sensing performance in a controlled way, it is essential to systematically construct relationships between the synthesis methods and the functions of the heteronanostructure for the sensing materials. In addition, the study of the surface reactions and the changes at the heterointerfaces by state-of-the-art characterization techniques can help elucidate their sensing mechanisms and provide guidelines for the design of heteronanostructure material-based sensors. Finally, exploring modern fabrication strategies of sensors may enable the implementation of wafer-scale fabrication of miniaturized gas sensors, which lead to their industrial applications.

Acknowledgements

We acknowledge the funding support from the National Key R&D Program of China (2018YFB1304700, 2017YFA0701101, 2020YFB2008501), the National Natural Science Foundation for Distinguished Young Scholars of China (No. 62125112), the National Natural Science Foundation of China (No. 62071462), Youth Promotion Association of Chinese Academy of Sciences (2020320), and

Suzhou Association for Science and Technology (E1391302). The authors are grateful for the technical support for Nano-X from Suzhou Institute of Nano-Tech and Nano-Bionics, Chinese Academy of Sciences (SINANO).

Author details

¹i-Lab, Key Laboratory of Multifunctional Nanomaterials and Smart Systems, Suzhou Institute of Nano-Tech and Nano-Bionics (SINANO), Chinese Academy of Sciences (CAS), Suzhou, Jiangsu, China. ²Department of Health and Environmental Sciences, Xi'an Jiaotong-Liverpool University, Suzhou, Jiangsu, China. ³Department of Nano Science and Nano Technology Institute, University of Science and Technology of China, Suzhou, Jiangsu, China. ⁴Nano-X, Suzhou Institute of Nano-Tech and Nano-Bionics (SINANO), Chinese Academy of Sciences (CAS), Suzhou, Jiangsu, China. ⁵School of Nano-Tech and Nano-Bionics, University of Science and Technology of China, Hefei, Anhui, PR China. ⁶Gusu Laboratory of Materials, Suzhou, Jiangsu, PR China. ⁷Center for Excellence in Brain Science and Intelligence Technology, Chinese Academy of Sciences, Shanghai, PR China

Conflict of interest

The authors declare no competing interests.

Received: 21 December 2021 Revised: 16 April 2022 Accepted: 20 May 2022
Published online: 28 July 2022

References

- Hansel, N. N. et al. A longitudinal study of indoor nitrogen dioxide levels and respiratory symptoms in inner-city children with asthma. *Environ. Health Perspect.* **116**, 1428–1432 (2008).
- Wellenius, G. A., Bateson, T. F., Mittleman, M. A. & Schwartz, J. Particulate air pollution and the rate of hospitalization for congestive heart failure among medicare beneficiaries in Pittsburgh, Pennsylvania. *Am. J. Epidemiol.* **161**, 1030–1036 (2005).
- Elliott, E. G. et al. Unconventional oil and gas development and risk of childhood leukemia: Assessing the evidence. *Sci. Total Environ.* **576**, 138–147 (2017).
- Yu, T. et al. Highly sensitive H₂S detection sensors at low temperature based on hierarchically structured NiO porous nanowall arrays. *J. Mater. Chem. A* **3**, 11991–11999 (2015).
- Institute, H. E. Start of Global air 2018, Special Report. (Boston, MA: Health Effects Institute, 2018).
- Peveler, W. J. et al. Multichannel Detection and Differentiation of Explosives with a Quantum Dot Array. *ACS Nano* **10**, 1139–1146 (2016).
- Freund, P., Senkowska, I. & Kaskel, S. Switchable conductive MOF-nanocarbon composite coatings as threshold sensing architectures. *ACS Appl. Mater. Interfaces* **9**, 43782–43789 (2017).
- Qu, J. et al. Transition-metal-doped p-type ZnO nanoparticle-based sensory array for instant discrimination of explosive vapors. *Small* **12**, 1369–1377 (2016).
- Choi, S. J. et al. Selective diagnosis of diabetes using Pt-functionalized WO₃ hemitube networks as a sensing layer of acetone in exhaled breath. *Anal. Chem.* **85**, 1792–1796 (2013).
- Nasiri, N. & Clarke, C. Nanostructured gas sensors for medical and health applications: low to high dimensional materials. *Biosensors* **9**, 43 (2019).
- Srinivasan, P. & Rayappan, J. B. B. Investigations on room temperature dual sensitization of ZnO nanostructures towards fish quality biomarkers. *Sens. Actuators, B* **304**, 127082 (2020).
- Srivastava, A. K., Dev, A. & Karmakar, S. Nanosensors and nanobiosensors in food and agriculture. *Environ. Chem. Lett.* **16**, 161–182 (2017).
- Masrie, M., Adnan, R., Ahmad, A. A hybrid gas sensor based on infrared absorption for indoor air quality monitoring. *Proceedings of the World Congress on Engineering* **2**, (2012).
- Werle, P. et al. Near-and mid-infrared laser-optical sensors for gas analysis. *Opt. Lasers Eng.* **37**, 101–114 (2002).
- Dey, A. Semiconductor metal oxide gas sensors: A review. *Mater. Sci. Eng., B* **229**, 206–217 (2018).
- Narayanan, S., Rice, G. & Agah, M. A micro-discharge photoionization detector for micro-gas chromatography. *Microchim. Acta* **181**, 493–499 (2013).
- Zimmer, C. M., Kallis, K. T. & Giebel, F. J. Micro-structured electron accelerator for the mobile gas ionization sensor technology. *J. Sens. Sens. Syst.* **4**, 151–157 (2015).
- Liu, J., Tan, Q., Xue, C. & Xiong, J. Design of a gas sensor for hydrazines based on photo-ionization principle. *Appl. Mech. Mater.* **44**, 2050–2054 (2011).
- SebtAhmadi, S. S. et al. General modeling and experimental observation of size dependence surface activity on the example of Pt nano-particles in electrochemical CO gas sensors. *Sens. Actuators, B* **285**, 310–316 (2019).
- Gębicki, J., Kloskowski, A. & Chrzanowski, W. Prototype of electrochemical sensor for measurements of volatile organic compounds in gases. *Sens. Actuators, B* **177**, 1173–1179 (2013).
- Dosi, M. et al. Ultrasensitive electrochemical methane sensors based on solid polymer electrolyte infused laser-induced graphene. *ACS Appl. Mater. Interfaces* **11**, 6166–6173 (2019).
- Struzik, M., Garbayo, I., Pfenninger, R. & Rupp, J. L. M. A simple and fast electrochemical CO₂ sensor based on Li₇La₃Zr₂O₁₂ for environmental monitoring. *Adv. Mater.* **30**, e1804098 (2018).
- Yang, M. et al. Preparation of highly crystalline NiO meshed nanowalls via ammonia volatilization liquid deposition for H₂S detection. *J. Colloid Interface Sci.* **540**, 39–50 (2019).
- Bao, F. et al. Photochemical Aging of Beijing Urban PM_{2.5}: HONO Production. *Environ. Sci. Technol.* **52**, 6309–6316 (2018).
- Korotcenkov, G. Metal oxides for solid-state gas sensors: What determines our choice? *Mater. Sci. Eng., B* **139**, 1–23 (2007).
- Neri, G., Donato, N. Resistive gas sensors. *Wiley encyclopedia of electrical and electronics engineering*, 1–12, (1999).
- Seiyama, T., Kato, A., Fujiishi, K. & Nagatani, M. A new detector for gaseous components using semiconductive thin films. *Anal. Chem.* **34**, 1502–1503 (1962).
- Neri, G. First Fifty Years of Chemoresistive Gas Sensors. *Chemosensors* **3**, 1–20 (2015).
- Hübner, M. et al. Influence of humidity on CO sensing with p-type CuO thick film gas sensors. *Sens. Actuators, B* **153**, 347–353 (2011).
- Kim, H. J. & Lee, J. H. Highly sensitive and selective gas sensors using p-type oxide semiconductors: Overview. *Sens. Actuators, B* **192**, 607–627 (2014).
- Song, Z. et al. Wireless self-powered high-performance integrated nanostructured-gas-sensor network for future smart homes. *ACS Nano* **15**, 7659–7667 (2021).
- Chen, J. et al. Ultra-low-power smart electronic nose system based on three-dimensional tin oxide nanotube arrays. *ACS Nano* **12**, 6079–6088 (2018).
- Pour, M. N., Nikfarjam, A., Taheri, A. & Sadredini, A. R. Gas sensor array assisted with UV illumination for discriminating several analytes at room temperature. *Micro Nano Lett.* **14**, 1064–1068 (2019).
- Hu, W. et al. Electronic noses: from advanced materials to sensors aided with data processing. *Adv. Mater. Technol.* **4**, 1800488 (2019).
- Zhang, B. & Gao, P. Metal oxide nanoarrays for chemical sensing: a review of fabrication methods, sensing modes, and their inter-correlations. *Front. Mater.* **6**, 55 (2019).
- Bulemo, P. M., Cho, H. J., Kim, N. H. & Kim, I. D. Mesoporous SnO₂ nanotubes via electrospinning-etching route: highly sensitive and selective detection of H₂S molecule. *ACS Appl. Mater. Interfaces* **9**, 26304–26313 (2017).
- Song, Z. et al. Nanosheet-assembled, hollowed-out hierarchical γ-Fe₂O₃ microrods for high-performance gas sensing. *J. Mater. Chem. A* **8**, 3754–3762 (2020).
- Meng, F. et al. UV-activated room temperature single-sheet ZnO gas sensor. *Micro Nano Lett.* **12**, 813–817 (2017).
- Kim, J. W. et al. Micropatternable double-faced ZnO nanoflowers for flexible gas sensor. *ACS Appl. Mater. Interfaces* **9**, 32876–32886 (2017).
- Bai, J. et al. Debye-length controlled gas sensing performances in NiO@ZnO p-n junctional core-shell nanotubes. *J. Phys. D: Appl. Phys.* **52**, 285103 (2019).
- Yuan, K. et al. Fabrication of a micro-electromechanical system-based acetone gas sensor using CeO₂ nanodot-decorated WO₃ nanowires. *ACS Appl. Mater. Interfaces* **12**, 14095–14104 (2020).
- Shao, S. et al. ZnO nanosheets modified with graphene quantum dots and SnO₂ quantum nanoparticles for room-temperature H₂S sensing. *ACS Appl. Nano Mater.* **3**, 5220–5230 (2020).
- Liu, X. et al. Nanoparticle cluster gas sensor: Pt activated SnO₂ nanoparticles for NH₃ detection with ultrahigh sensitivity. *Nanoscale* **7**, 14872–14880 (2015).

44. Majhi, S. M. et al. Au@NiO core-shell nanoparticles as a p-type gas sensor: Novel synthesis, characterization, and their gas sensing properties with sensing mechanism. *Sens. Actuators, B* **268**, 223–231 (2018).
45. Kim, J. D., Yun, J. H., Song, J. W. & Han, C. S. The spontaneous metal-sitting structure on carbon nanotube arrays positioned by inkjet printing for wafer-scale production of high sensitive gas sensor units. *Sens. Actuators, B* **135**, 587–591 (2009).
46. Feng, Q., Li, X. & Wang, J. Percolation effect of reduced graphene oxide (rGO) on ammonia sensing of rGO-SnO₂ composite based sensor. *Sens. Actuators, B* **243**, 1115–1126 (2017).
47. Siddiqui, G. U. et al. Wide range highly sensitive relative humidity sensor based on series combination of MoS₂ and PEDOT:PSS sensors array. *Sens. Actuators, B* **266**, 354–363 (2018).
48. Wang, K. et al. Inorganic–organic pn heterojunction nanotree arrays for a high-sensitivity diode humidity sensor. *ACS Appl. Mater. Interfaces* **5**, 5825–5831 (2013).
49. Yuan, H. et al. ZnO nanosheets abundant in oxygen vacancies derived from metal-organic frameworks for ppb-level gas sensing. *Adv. Mater.* **31**, 1807161 (2019).
50. Gui, Y. et al. P-type Co₃O₄ nanoarrays decorated on the surface of n-type flower-like WO₃ nanosheets for high-performance gas sensing. *Sens. Actuators, B* **288**, 104–112 (2019).
51. Zhang, Z. et al. Novel SnO₂@ZnO hierarchical nanostructures for highly sensitive and selective NO₂ gas sensing. *Sens. Actuators, B* **257**, 714–727 (2018).
52. Liu, L. et al. In situ growth of NiO@SnO₂ hierarchical nanostructures for high performance H₂S sensing. *ACS Appl. Mater. Interfaces* **11**, 44829–44836 (2019).
53. Zhang, S. et al. An acetone gas sensor based on nanosized Pt-loaded Fe₂O₃ nanocubes. *Sens. Actuators, B* **290**, 59–67 (2019).
54. Li, H. et al. Multilevel effective heterojunctions based on SnO₂/ZnO 1D fibrous hierarchical structure with unique interface electronic effects. *ACS Appl. Mater. Interfaces* **11**, 31551–31561 (2019).
55. Miller, D. R., Akbar, S. A. & Morris, P. A. Nanoscale metal oxide-based heterojunctions for gas sensing: a review. *Sens. Actuators, B* **204**, 250–272 (2014).
56. Zappa, D. et al. "Metal oxide -based heterostructures for gas sensors"- a review. *Anal. Chim. Acta* **1039**, 1–23 (2018).
57. Mercante, L. A., Andre, R. S., Mattoso, L. H. C. & Correa, D. S. Electrospun ceramic nanofibers and hybrid-nanofiber composites for gas sensing. *ACS Appl. Nano Mater.* **2**, 4026–4042 (2019).
58. Yu, H. et al. Spatial variation of surface water quality in Hangzhou section of Qiantang river during different water periods. *Yellow River*, 08, (2016).
59. Li, Z. et al. Advances in designs and mechanisms of semiconducting metal oxide nanostructures for high-precision gas sensors operated at room temperature. *Mater. Horiz.* **6**, 470–506 (2019).
60. Ahmad, R. et al. Recent progress and perspectives of gas sensors based on vertically oriented ZnO nanomaterials. *Adv. Colloid Interface Sci.* **270**, 1–27 (2019).
61. Yulianto, B., Gumilar, G. & Septiani, N. L. W. SnO₂ nanostructure as pollutant gas sensors: synthesis, sensing performances, and mechanism. *Adv. Mater. Sci. Eng.* **2015**, 1–14 (2015).
62. Gurlo, A. Nanosensors: towards morphological control of gas sensing activity. SnO₂, In₂O₃, ZnO and WO₃ case studies. *Nanoscale* **3**, 154–165 (2011).
63. Koo, W. T. et al. Chemiresistive hydrogen sensors: fundamentals, recent advances, and challenges. *ACS Nano* **14**, 14284–14322 (2020).
64. Al-Hashem, M., Akbar, S. & Morris, P. Role of oxygen vacancies in nanostructured metal-oxide gas sensors: a review. *Sens. Actuators, B* **301**, 126845 (2019).
65. Ji, H., Zeng, W. & Li, Y. Gas sensing mechanisms of metal oxide semiconductors: a focus review. *Nanoscale* **11**, 22664–22684 (2019).
66. Chen, S., Gao, N., Bunes, B. R. & Zang, L. Tunable nanofibril heterojunctions for controlling interfacial charge transfer in chemiresistive gas sensors. *J. Mater. Chem. C* **7**, 13709–13735 (2019).
67. Wang, B., Nisar, J. & Ahuja, R. Molecular simulation for gas adsorption at NiO (100) surface. *ACS Appl. Mater. Interfaces* **4**, 5691–5697 (2012).
68. Kida, T. et al. Pore and particle size control of gas sensing films using SnO₂ nanoparticles synthesized by seed-mediated growth: design of highly sensitive gas sensors. *J. Phys. Chem. C* **117**, 17574–17582 (2013).
69. Bulemo, P. M., Cho, H. J., Kim, D. H. & Kim, I. D. Facile synthesis of Pt-functionalized meso/macroporous SnO₂ hollow spheres through in situ templating with SiO₂ for H₂S sensors. *ACS Appl. Mater. Interfaces* **10**, 18183–18191 (2018).
70. Wang, Y. et al. Sputtered SnO₂/NiO thin films on self-assembled Au nanoparticle arrays for MEMS compatible NO₂ gas sensors. *Sens. Actuators, B* **278**, 28–38 (2019).
71. Xu, C., Tamaki, J., Miura, N. & Yamazoe, N. Grain size effects on gas sensitivity of porous SnO₂-based elements. *Sens. Actuators, B* **3**, 147–155 (1991).
72. Cui, S. et al. Ultrasensitive chemical sensing through facile tuning defects and functional groups in reduced graphene oxide. *Anal. Chem.* **86**, 7516–7522 (2014).
73. Bandara, N., Jayatilaka, C., Dissanayaka, D. & Jayanetti, S. Temperature effects on gas sensing properties of electrodeposited chlorine doped and undoped n-type cuprous oxide thin films. *J. Sens. Technol.* **04**, 119–126 (2014).
74. Gad, A. et al. Integrated strategy toward self-powering and selectivity tuning of semiconductor gas sensors. *ACS Sens* **1**, 1256–1264 (2016).
75. Liu, L. et al. A photovoltaic self-powered gas sensor based on a single-walled carbon nanotube/Si heterojunction. *Nanoscale* **9**, 18579–18583 (2017).
76. Jose, A. S., Prajwal, K., Chowdhury, P. & Barshilia, H. C. Sputter deposited p-NiO/n-SnO₂ porous thin film heterojunction based NO₂ sensor with high selectivity and fast response. *Sens. Actuators, B* **310**, 127830 (2020).
77. Kumar, A., Sanger, A., Kumar, A. & Chandra, R. Fast response ammonia sensors based on TiO₂ and NiO nanostructured bilayer thin films. *RSC Adv.* **6**, 77636–77643 (2016).
78. Barsan, N., Koziej, D. & Weimar, U. Metal oxide-based gas sensor research: How to? *Sens. Actuators, B* **121**, 18–35 (2007).
79. Batzill, M. & Diebold, U. The surface and materials science of tin oxide. *Prog. Surf. Sci.* **79**, 47–154 (2005).
80. Lee, J.-H. Gas sensors using hierarchical and hollow oxide nanostructures: overview. *Sens. Actuators, B* **140**, 319–336 (2009).
81. Comini, E. et al. Stable and highly sensitive gas sensors based on semiconducting oxide nanobelts. *Appl. Phys. Lett.* **81**, 1869–1871 (2002).
82. Sun, G. J. et al. H₂S gas sensing properties of Fe₂O₃ nanoparticle-decorated NiO nanoplate sensors. *Surf. Coat. Technol.* **307**, 1088–1095 (2016).
83. Zhou, X. et al. Crystal-defect-dependent gas-sensing mechanism of the single ZnO nanowire sensors. *ACS Sens* **3**, 2385–2393 (2018).
84. Choi, P. G., Fuchigami, T., Kakimoto, K.-I. & Masuda, Y. Effect of crystal defect on gas sensing properties of Co₃O₄ nanoparticles. *ACS Sens* **5**, 1665–1673 (2020).
85. Motaung, D. E. et al. Ultra-high sensitive and selective H₂ gas sensor manifested by interface of n-n heterostructure of CeO₂-SnO₂ nanoparticles. *Sens. Actuators, B* **254**, 984–995 (2018).
86. Wang, X. et al. Controlled synthesis and enhanced catalytic and gas-sensing properties of tin dioxide nanoparticles with exposed high-energy facets. *Chem. Eur. J.* **18**, 2283–2289 (2012).
87. Bi, H. et al. Morphology-controlled synthesis of CeO₂ nanocrystals and their facet-dependent gas sensing properties. *Sens. Actuators, B* **330**, 129374 (2021).
88. Han, X. et al. Synthesis of tin dioxide octahedral nanoparticles with exposed high-energy {221} facets and enhanced gas-sensing properties. *Angew. Chem., Int. Ed.* **48**, 9180–9183 (2009).
89. Yamazoe, N. Toward innovations of gas sensor technology. *Sens. Actuators, B* **108**, 2–14 (2005).
90. Katoch, A., Abideen, Z. U., Kim, H. W. & Kim, S. S. Grain-size-tuned highly H₂-selective chemiresistive sensors based on ZnO-SnO₂ composite nanofibers. *ACS Appl. Mater. Interfaces* **8**, 2486–2494 (2016).
91. Wang, L. et al. Grain-boundary-induced drastic sensing performance enhancement of polycrystalline-microwire printed gas sensors. *Adv. Mater.* **31**, 1804583 (2019).
92. Sakai, G., Matsunaga, N., Shimanoe, K. & Yamazoe, N. Theory of gas-diffusion controlled sensitivity for thin film semiconductor gas sensor. *Sens. Actuators, B* **80**, 125–131 (2001).
93. Shimanoe, K., Yuasa, M., Kida, T., Yamazoe, N. In *2011 IEEE Nanotechnology Materials and Devices Conference*. 38–43 (IEEE).
94. Adamu, B. I. et al. p-p heterojunction sensors of p-Cu₃Mo₂O₉ micro/nanorods vertically grown on p-CuO layers for room-temperature ultrasensitive and fast recoverable detection of NO₂. *ACS Appl. Mater. Interfaces* **12**, 8411–8421 (2020).
95. Yan, W. et al. MOF-derived porous hollow Co₃O₄@ZnO cages for high-performance MEMS trimethylamine sensors. *ACS Sens* **6**, 2613–2621 (2021).
96. Lou, C. et al. Fe₂O₃-sensitized SnO₂ nanosheets via atomic layer deposition for sensitive formaldehyde detection. *Sens. Actuators, B* **345**, 130429 (2021).

97. Zhang, R. et al. Rational design and tunable synthesis of Co_3O_4 nanoparticle-incorporating into In_2O_3 one-dimensional ribbon as effective sensing material for gas detection. *Sens. Actuators, B* **310**, (2020).
98. Kim, J. H. et al. Optimization and gas sensing mechanism of n-SnO₂-p-Co₃O₄ composite nanofibers. *Sens. Actuators, B* **248**, 500–511 (2017).
99. Kim, J. H. et al. Enhancement of CO and NO₂ sensing in n-SnO₂-p-Cu₂O core-shell nanofibers by shell optimization. *J. Hazard. Mater.* **376**, 68–82 (2019).
100. Kim, J. H. & Kim, S. S. Realization of ppb-Scale toluene-sensing abilities with Pt-functionalized SnO₂-ZnO core-shell nanowires. *ACS Appl. Mater. Interfaces* **7**, 17199–17208 (2015).
101. Walker, J. M., Akbar, S. A. & Morris, P. A. Synergistic effects in gas sensing semiconducting oxide nano-heterostructures: a review. *Sens. Actuators, B* **286**, 624–640 (2019).
102. Naik, A., Parkin, I. & Binions, R. Gas sensing studies of an n-n hetero-junction array based on SnO₂ and ZnO. *Compos. Chemosens.* **4**, 3 (2016).
103. Li, B. et al. Core-shell structure of ZnO/Co₃O₄ composites derived from bimetallic-organic frameworks with superior sensing performance for ethanol gas. *Appl. Surf. Sci.* **475**, 700–709 (2019).
104. Mulmi, S. & Thangadurai, V. Semiconducting SnO₂-TiO₂ (ST) composites for detection of SO₂ gas. *Ionics* **22**, 1927–1935 (2016).
105. Li, S. et al. Metal-Organic frameworks-derived bamboo-like CuO/In₂O₃ Heterostructure for high-performance H₂S gas sensor with Low operating temperature. *Sens. Actuators, B* **310**, 127828 (2020).
106. Xiong, Y. et al. ZIF-derived porous ZnO-Co₃O₄ hollow polyhedrons heterostructure with highly enhanced ethanol detection performance. *Sens. Actuators, B* **253**, 523–532 (2017).
107. Wei, Q. et al. Spindle-like Fe₂O₃/ZnFe₂O₄ porous nanocomposites derived from metal-organic frameworks with excellent sensing performance towards triethylamine. *Sens. Actuators, B* **317**, 128205 (2020).
108. Liu, D., Wan, J., Pang, G. & Tang, Z. Hollow metal-organic-framework micro/nanostructures and their derivatives: emerging multifunctional materials. *Adv. Mater.* **31**, 1803291 (2019).
109. Gao, X. et al. Porous MoO₃/SnO₂ Nanoflakes with n-n Junctions for Sensing H₂S. *ACS Appl. Nano Mater.* **2**, 2418–2425 (2019).
110. Shaposhnik, D. et al. Hydrogen sensors on the basis of SnO₂-TiO₂ systems. *Sens. Actuators, B* **174**, 527–534 (2012).
111. Staerz, A. et al. Dominant role of heterojunctions in gas sensing with composite materials. *ACS Appl. Mater. Interfaces* **12**, 21127–21132 (2020).
112. Yamazoe, N. & Shimanoe, K. Basic approach to the transducer function of oxide semiconductor gas sensors. *Sens. Actuators, B* **160**, 1352–1362 (2011).
113. Yamazoe, N. & Shimanoe, K. Proposal of contact potential promoted oxide semiconductor gas sensor. *Sens. Actuators, B* **187**, 162–167 (2013).
114. Xu, Y. et al. p-p heterojunction composite of NiFe₂O₄ nanoparticles-decorated NiO nanosheets for acetone gas detection. *Mater. Lett.* **270**, 127728 (2020).
115. Dong, S. et al. Multi-dimensional templated synthesis of hierarchical Fe₂O₃/NiO composites and their superior ethanol sensing properties promoted by nanoscale p-n heterojunctions. *Dalton Trans.* **49**, 1300–1310 (2020).
116. Yoon, J. W. et al. Kilogram-scale synthesis of Pd-loaded quintuple-shelled Co₃O₄ microreactors and their application to ultrasensitive and ultraspecific detection of methylbenzenes. *ACS Appl. Mater. Interfaces* **7**, 7717–7723 (2015).
117. Huo, L. et al. Modulation of potential barrier heights in Co₃O₄/SnO₂ heterojunctions for highly H₂-selective sensors. *Sens. Actuators, B* **244**, 694–700 (2017).
118. Yin, X.-T. et al. Ultra-high selectivity of H₂ over CO with a p-n nanojunction based gas sensors and its mechanism. *Sens. Actuators, B* **319**, 128330 (2020).
119. Katoch, A. et al. Bifunctional sensing mechanism of SnO₂-ZnO composite nanofibers for drastically enhancing the sensing behavior in H₂ gas. *ACS Appl. Mater. Interfaces* **7**, 11351–11358 (2015).
120. Wang, C. et al. Hydrogen-induced metallization of zinc oxide (2(11)over-bar-0) surface and nanowires: the effect of curvature. *Phys. Rev. B* **77**, 245303 (2008).
121. Wang, Y. et al. Hydrogen Induced Metallicity on the ZnO (1010) Surface. *Phys. Rev. Lett.* **95**, 266104 (2005).
122. Ramakrishnan, V. et al. Porous, n-p type ultra-long, ZnO@Bi₂O₃ heterojunction nanorods-based NO₂ gas sensor: new insights towards charge transport characteristics. *Phys. Chem. Chem. Phys.* **22**, 7524–7536 (2020).
123. Ju, D. X. et al. Near room temperature, fast-response, and highly sensitive triethylamine sensor assembled with Au-loaded ZnO/SnO₂ core-shell nanorods on flat alumina substrates. *ACS Appl. Mater. Interfaces* **7**, 19163–19171 (2015).
124. Suematsu, K. et al. Ultrasensitive toluene-gas sensor: nanosized gold loaded on zinc oxide nanoparticles. *Anal. Chem.* **90**, 1959–1966 (2018).
125. Gunawan, P. et al. Ultrahigh sensitivity of Au/1D α -Fe₂O₃ to acetone and the sensing mechanism. *Langmuir* **28**, 14090–14099 (2012).
126. Kim, S. J. et al. Exceptional high-performance of Pt-based bimetallic catalysts for exclusive detection of exhaled biomarkers. *Adv. Mater.* **29**, 1700737 (2017).
127. Wang, K., Wang, X. & Liang, X. Synthesis of high metal loading single atom catalysts and exploration of the active center structure. *ChemCatChem* **12**, 1–32 (2020).
128. Ou, H., Wang, D. & Li, Y. How to select effective electrocatalysts: Nano or single atom? *Nano Sel.* **2**, 492–511 (2021).
129. Shin, H. et al. Single-atom Pt stabilized on one-dimensional nanostructure support via carbon nitride/SnO₂ heterojunction trapping. *ACS Nano* **14**, 11394–11405 (2020).
130. Wang, Y. et al. In operando impedance spectroscopic analysis on NiO-WO₃ nanorod heterojunction random networks for room-temperature H₂S detection. *ACS Omega* **3**, 18685–18693 (2018).
131. Choi, S. W., Katoch, A., Kim, J. H. & Kim, S. S. Prominent reducing gas-sensing performances of n-SnO₂ nanowires by local creation of p-n heterojunctions by functionalization with p-Cr₂O₃ nanoparticles. *ACS Appl. Mater. Interfaces* **6**, 17723–17729 (2014).
132. Song, Y. G. et al. Heterojunction based on Rh-decorated WO₃ nanorods for morphological change and gas sensor application using the transition effect. *Chem. Mater.* **31**, 207–215 (2018).
133. Choi, S. W., Katoch, A., Kim, J. H. & Kim, S. S. Striking sensing improvement of n-type oxide nanowires by electronic sensitization based on work function difference. *J. Mater. Chem. C* **3**, 1521–1527 (2015).
134. Wang, J. et al. Hierarchical ZnO nanosheet-nanorod architectures for fabrication of poly (3-hexylthiophene)/ZnO hybrid NO₂ sensor. *ACS Appl. Mater. Interfaces* **8**, 8600–8607 (2016).
135. Wei, Z. et al. Ultra-thin sub-10 nm Ga₂O₃-WO₃ heterostructures developed by atomic layer deposition for sensitive and selective C₂H₅OH detection on ppm level. *Sens. Actuators, B* **287**, 147–156 (2019).
136. Maziarz, W. TiO₂/SnO₂ and TiO₂/CuO thin film nano-heterostructures as gas sensors. *Appl. Surf. Sci.* **480**, 361–370 (2019).
137. Fang, J. et al. Gas sensing properties of NiO/SnO₂ heterojunction thin film. *Sens. Actuators, B* **252**, 1163–1168 (2017).
138. Wang, J., Yang, P. & Wei, X. High-performance, room-temperature, and no-humidity-impact ammonia sensor based on heterogeneous nickel oxide and zinc oxide nanocrystals. *ACS Appl. Mater. Interfaces* **7**, 3816–3824 (2015).
139. Zhu, L. et al. Hierarchical highly ordered SnO₂ nanobowl branched ZnO nanowires for ultrasensitive and selective hydrogen sulfide gas sensing. *Microsyst. Nanoeng.* **6**, 1–13 (2020).
140. Saravanan, A., Huang, B. R., Kathiravan, D. & Prasannan, A. Natural biowaste-coconut-derived granular activated carbon-coated ZnO nanorods: a simple route to synthesizing a core-shell structure and its highly enhanced uv and hydrogen sensing properties. *ACS Appl. Mater. Interfaces* **9**, 39771–39780 (2017).
141. Cao, J. et al. Core-shell Co₃O₄/ α -Fe₂O₃ heterostructure nanofibers with enhanced gas sensing properties. *RSC Adv.* **5**, 36340–36346 (2015).
142. Liu, D. et al. Low power consumption gas sensor created from silicon nanowires/TiO₂ core-shell heterojunctions. *ACS Sens.* **2**, 1491–1497 (2017).
143. Li, F., Gao, X., Wang, R. & Zhang, T. Design of WO₃-SnO₂ core-shell nanofibers and their enhanced gas sensing performance based on different work function. *Appl. Surf. Sci.* **442**, 30–37 (2018).
144. Xu, Q. et al. Improving the triethylamine sensing performance based on debye length: A case study on α -Fe₂O₃@NiO(CuO) core-shell nanorods sensor working at near room-temperature. *Sens. Actuators, B* **245**, 375–385 (2017).
145. Choi, S. W. et al. Dual functional sensing mechanism in SnO₂-ZnO core-shell nanowires. *ACS Appl. Mater. Interfaces* **6**, 8281–8287 (2014).
146. Kim, J. H., Katoch, A., Kim, S. H. & Kim, S. S. Chemiresistive sensing behavior of SnO₂ (n)-Cu₂O (p) core-shell nanowires. *ACS Appl. Mater. Interfaces* **7**, 15351–15358 (2015).
147. Mirzaei, A., Kim, J. H., Kim, H. W. & Kim, S. S. How shell thickness can affect the gas sensing properties of nanostructured materials: survey of literature. *Sens. Actuators, B* **258**, 270–294 (2018).
148. Lee, J. H., Kim, J. H. & Kim, S. S. CuO-TiO₂ p-n core-shell nanowires: Sensing mechanism and p/n sensing-type transition. *Appl. Surf. Sci.* **448**, 489–497 (2018).

149. Zhu, L.-Y. et al. Fabrication of heterostructured p-CuO/n-SnO₂ core-shell nanowires for enhanced sensitive and selective formaldehyde detection. *Sens. Actuators, B* **290**, 233–241 (2019).
150. Zhou, T. et al. Constructing hierarchical heterostructured Mn₃O₄/Zn₂SnO₄ materials for efficient gas sensing reaction. *Adv. Mater. Interfaces* **5**, 1800115 (2018).
151. Kaur, N. et al. Branch-like NiO/ZnO heterostructures for VOC sensing. *Sens. Actuators, B* **262**, 477–485 (2018).
152. Hao, L. et al. Flexible Pd-WSe₂/Si heterojunction sensors for highly sensitive detection of hydrogen at room temperature. *Sens. Actuators, B* **283**, 740–748 (2019).
153. Wang, C. et al. In situ synthesis of flower-like ZnO on GaN using electro-deposition and its application as ethanol gas sensor at room temperature. *Sens. Actuators, B* **292**, 270–276 (2019).
154. Xie, C. et al. Core-shell heterojunction of silicon nanowire arrays and carbon quantum dots for photovoltaic devices and self-driven photodetectors. *ACS Nano* **8**, 4015–4022 (2014).
155. Reddeppa, M. et al. NO_x gas sensors based on layer-transferred n-MoS₂/p-GaN heterojunction at room temperature: study of UV light illuminations and humidity. *Sens. Actuators, B* **308**, 127700 (2020).
156. Sze, S. M., Li, Y., Ng, K. K. *Physics of semiconductor devices*. (John Wiley & sons, 2021).
157. Kwon, H. et al. An array of metal oxides nanoscale hetero pn junctions toward designable and highly-selective gas sensors. *Sens. Actuators, B* **255**, 1663–1670 (2018).
158. Xu, F. & Ho, H. P. Light-activated metal oxide gas sensors: a review. *Micro-machines* **8**, 333 (2017).
159. Liu, X. et al. Light stimulated and regulated gas sensing ability for ammonia using sulfur-hyperdoped silicon. *Sens. Actuators, B* **291**, 345–353 (2019).
160. Hoffmann, M. W. G. et al. Solar diode sensor: Sensing mechanism and applications. *Nano Energy* **2**, 514–522 (2013).
161. Hoffmann, M. W. G. et al. A highly selective and self-powered gas sensor via organic surface functionalization of p-Si/n-ZnO diodes. *Adv. Mater.* **26**, 8017–8022 (2014).
162. Tanuma, R. & Sugiyama, M. Polycrystalline SnO₂ visible-light-transparent CO₂ sensor integrated with NiO/ZnO solar cell for self-powered devices. *Phys. Status Solidi A* **216**, 1800749 (2019).
163. Baranov, A., Spirjakin, D., Akbari, S. & Somov, A. Optimization of power consumption for gas sensor nodes: a survey. *Sens. Actuators, A* **233**, 279–289 (2015).
164. Zhou, Q. et al. Fast response integrated MEMS microheaters for ultra low power gas detection. *Sens. Actuators, A* **223**, 67–75 (2015).
165. Khairul, M. A. et al. Effects of surfactant on stability and thermo-physical properties of metal oxide nanofluids. *Int. J. Heat. Mass Transf.* **98**, 778–787 (2016).
166. Jiao, Z., Wang, S., Bian, L. & Liu, J. Stability of SnO₂/Fe₂O₃ multilayer thin film gas sensor. *Mater. Res. Bull.* **35**, 741–745 (2000).
167. Yang, S. et al. Au@ZnO functionalized three-dimensional macroporous WO₃: a application of selective H₂S gas sensor for exhaled breath biomarker detection. *Sens. Actuators, B* **324**, 128725 (2020).
168. Xu, K. et al. Single-crystalline porous nanosheets assembled hierarchical Co₃O₄ microspheres for enhanced gas-sensing properties to trace xylene. *Sens. Actuators, B* **246**, 68–77 (2017).
169. Jeong, S.-Y., Kim, J.-S. & Lee, J.-H. Rational design of semiconductor-based chemiresistors and their libraries for next-generation artificial olfaction. *Adv. Mater.* **32**, 2002075 (2020).
170. Yadav, A. B. & Jit, S. Particle size effects on the hydrogen sensing properties of Pd/ZnO Schottky contacts fabricated by sol-gel method. *Int. J. Hydrog. Energy* **42**, 786–794 (2017).
171. Tian, H., Fan, H., Li, M. & Ma, L. Zeolitic imidazolate framework coated ZnO nanorods as molecular sieving to improve selectivity of formaldehyde gas sensor. *ACS Sens* **1**, 243–250 (2016).
172. Drobek, M. et al. MOF-based membrane encapsulated ZnO nanowires for enhanced gas sensor selectivity. *ACS Appl. Mater. Interfaces* **8**, 8323–8328 (2016).
173. Niu, G. et al. NiO nanoparticle-decorated SnO₂ nanosheets for ethanol sensing with enhanced moisture resistance. *Microsyst. Nanoeng.* **5**, 1–8 (2019).
174. Liu, L. et al. “Top-down” and “bottom-up” strategies for wafer-scaled miniaturized gas sensors design and fabrication. *Microsyst. Nanoeng.* **6** (2020).
175. Degler, D. et al. Platinum loaded tin dioxide: a model system for unravelling the interplay between heterogeneous catalysis and gas sensing. *J. Mater. Chem. A* **6**, 2034–2046 (2018).
176. Barsan, N. & Weimar, U. Conduction model of metal oxide gas sensors. *J. Electroceram* **7**, 143–167 (2001).
177. Groves, W. A. & Zellers, E. T. Analysis of solvent vapors in breath and ambient air with a surface acoustic wave sensor array. *Ann. Occup. Hyg.* **45**, 609–623 (2001).
178. Konvalina, G. & Haick, H. Effect of humidity on nanoparticle-based chemiresistors: a comparison between synthetic and real-world samples. *ACS Appl. Mater. Interfaces* **4**, 317–325 (2012).
179. Wu, J. et al. 3D superhydrophobic reduced graphene oxide for activated NO₂ sensing with enhanced immunity to humidity. *J. Mater. Chem. A* **6**, 478–488 (2018).
180. Huang, Y. et al. High sensitivity, humidity-independent, flexible NO₂ and NH₃ gas sensors based on SnS₂ hybrid functional graphene ink. *ACS Appl. Mater. Interfaces* **12**, 997–1004 (2020).
181. Ma, N. et al. Effect of water vapor on Pd-loaded SnO₂ nanoparticles gas sensor. *ACS Appl. Mater. Interfaces* **7**, 5863–5869 (2015).
182. Kim, H. R. et al. The role of NiO doping in reducing the impact of humidity on the performance of SnO₂-Based gas sensors: synthesis strategies, and phenomenological and spectroscopic studies. *Adv. Funct. Mater.* **21**, 4456–4463 (2011).
183. Choi, K. I., Kim, H. J., Kang, Y. C. & Lee, J. H. Ultrasensitive and ultrasensitive detection of H₂S in highly humid atmosphere using CuO-loaded SnO₂ hollow spheres for real-time diagnosis of halitosis. *Sens. Actuators, B* **194**, 371–376 (2014).
184. Yao, M. S. et al. MOF thin film-coated metal oxide nanowire array: significantly improved chemiresistor sensor performance. *Adv. Mater.* **28**, 5229–5234 (2016).
185. Wang, Y. et al. Humidity-Insensitive NO₂ Sensors Based on SnO₂/rGO Composites. *Front. Chem.* **9**, (2021).
186. Liu, J. et al. Size effect and comprehensive mathematical model for gas-sensing mechanism of SnO₂ thin film gas sensors. *J. Alloy. Compd.* **898**, 162875 (2022).
187. Sun, Y. et al. The effect of Zeolite composition and grain size on gas sensing properties of SnO₂/Zeolite sensor. *Sensors* **18**, 390 (2018).
188. Chen, Y. et al. ZnO-nanowire size effect induced ultra-high sensing response to ppb-level H₂S. *Sens. Actuators B* **240**, 264–272 (2017).
189. Wang, L., Cao, J., Qian, X. & Zhang, H. Facile synthesis and enhanced gas sensing properties of grain size-adjustable In₂O₃ micro/nanotubes. *Mater. Lett.* **171**, 30–33 (2016).
190. Jin, C. et al. Influence of nanoparticle size on ethanol gas sensing performance of mesoporous α-Fe₂O₃ hollow spheres. *Mater. Sci. Eng. B* **224**, 158–162 (2017).
191. Han, M. A. et al. Effects of porosity and particle size on the gas sensing properties of SnO₂ films. *Appl. Surf. Sci.* **481**, 133–137 (2019).
192. Lou, Z. et al. Toluene and ethanol sensing performances of pristine and PdO-decorated flower-like ZnO structures. *Sens. Actuators B* **176**, 323–329 (2013).
193. Wang, Z. et al. α-Fe₂O₃/NiO heterojunction nanorods with enhanced gas sensing performance for acetone. *Sens. Actuators, B* **318**, 128191 (2020).
194. Gong, F.-L. et al. Design of pn heterojunction on mesoporous ZnO/Co₃O₄ nanosheets for triethylamine sensor. *Chem. Phys. Lett.* **779**, 138891 (2021).
195. Wang, Z. et al. Construction of ZnO/SnO₂ heterostructure on reduced graphene oxide for enhanced nitrogen dioxide sensitive performances at room temperature. *ACS Sens* **4**, 2048–2057 (2019).
196. Choi, K. et al. Effects of particle size on the NO₂ gas sensing properties of NiO nanoparticle-decorated SnO₂ nanorods. *J. Korean Phys. Soc.* **77**, 482–488 (2020).
197. Zhang, L. & Yin, Y. Large-scale synthesis of flower-like ZnO nanorods via a wet-chemical route and the defect-enhanced ethanol-sensing properties. *Sens. Actuators B* **183**, 110–116 (2013).
198. Wei, W. et al. Enhancing triethylamine sensing of ZIF-derived ZnO microspheres arising from cobalt doping and defect engineering. *Chemosphere* **291**, 132715 (2022).
199. Gu, F. et al. Improvement of gas-sensing property by defect engineering in microwave-assisted synthesized 3D ZnO nanostructures. *Sens. Actuators B* **204**, 342–350 (2014).
200. Zhang, L.-X. et al. Rich defects and nanograins boosted formaldehyde sensing performance of mesoporous polycrystalline ZnO nanosheets. *Rare Metals*, 1–13, (2022).

201. Zhang, H. et al. Extending the detection range and response of TiO₂ based hydrogen sensors by surface defect engineering. *Int. J. Hydrog. Energy* **45**, 18057–18065 (2020).
202. Wang, X. et al. Oxygen vacancy defects engineering on Ce-doped α -Fe₂O₃ gas sensor for reducing gases. *Sens. Actuators, B* **302**, 127165 (2020).
203. Chen, Y. et al. Interface defect engineering induced drastic sensing performance enhancement of W₁₈O₄₉@PANI nanowires for ammonia detection at room temperature. *Appl. Surf. Sci.* **506**, 144816 (2020).
204. Luo, N. et al. Ultralow detection limit MEMS hydrogen sensor based on SnO₂ with oxygen vacancies. *Sens. Actuators, B* **354**, 130982 (2022).
205. Wang, L. et al. Mo-doped SnO₂ nanotubes sensor with abundant oxygen vacancies for ethanol detection. *Sens. Actuators, B* **347**, 130642 (2021).
206. Wang, L. et al. Oxygen vacancy-based Tb-doped SnO₂ nanotubes as an ultrasensitive sensor for ethanol detection. *Sens. Actuators, B* **344**, 130111 (2021).
207. Wang, Z. et al. Ultrasensitive NO₂ gas sensor based on Sb-doped SnO₂ covered ZnO nano-heterojunction. *J. Mater. Sci.* **56**, 7348–7356 (2021).
208. Zhang, L. et al. Facile one-step hydrothermal synthesis of SnO₂ microspheres with oxygen vacancies for superior ethanol sensor. *J. Alloy. Compd.* **814**, 152266 (2020).
209. Qin, Y. et al. Enhanced gas sensing performance of Bi₂MoO₆ with introduction of oxygen vacancy: coupling of experiments and first-principles calculations. *J. Alloy. Compd.* **894**, 162534 (2022).
210. Liu, J. et al. Controllable synthesis of In₂O₃ octahedra exposing {110} facets with enhanced gas sensing performance. *RSC Adv.* **5**, 44306–44312 (2015).
211. Xu, J. et al. The crystal facet-dependent gas sensing properties of ZnO nanosheets: experimental and computational study. *Sens. Actuators, B* **242**, 148–157 (2017).
212. Xu, R. et al. Ultrathin SnO₂ nanosheets with dominant high-energy {001} facets for low temperature formaldehyde gas sensor. *Sens. Actuators, B* **289**, 186–194 (2019).
213. Sun, H. & Lv, H. Facet engineering of Nano-Co₃O₄ for catalytic and gas sensor performance: a mechanism insight. *J. Alloy. Compd.* **823**, 153742 (2020).
214. Choi, P. G., Izu, N., Shirahata, N. & Masuda, Y. SnO₂ nanosheets for selective alkene gas sensing. *ACS Appl. Nano Mater.* **2**, 1820–1827 (2019).
215. Zhang, N. et al. Synthesis of Au-decorated SnO₂ crystallites with exposed {221} facets and their enhanced acetylene sensing properties. *Sens. Actuators, B* **307**, 127629 (2020).